Interplay of deformability and adhesion on localization of elastic micro-particles in blood flow

Huilin Ye[1], Zhiqiang Shen[1] and Ying Li[12]†

[1]Department of Mechanical Engineering, University of Connecticut, 191 Auditorium Road, Unit 3139, Storrs, Connecticut 06269, United States

[2]Institute of Materials Science, University of Connecticut, 97 North Eagleville Road, Unit 3136, Storrs, Connecticut 06269, United States

(Received xx; revised xx; accepted xx)

The margination and adhesion of micro-particles (MPs) have been extensively investigated separately, due to their important applications in biomedical field. However, the cascade process from margination to adhesion should play an important role in the transport of MPs in blood flow. To the best of our knowledge, it has not been explored in the past. Here we numerically study the margination behavior of elastic MPs to blood vessel wall under the interplay of their deformability and adhesion to vessel wall. We use the Lattice Boltzmann method (LBM) and molecular dynamics to solve fluid dynamics and particle (including red blood cells (RBCs) and elastic MPs) dynamics in blood flow, respectively. Additionally, a stochastic ligand-receptor binding model is employed to capture the adhesion behaviors of elastic MPs on the vessel wall. Margination probability is used to quantify the localization of elastic MPs at wall. Two dimensionless numbers are considered to govern the whole process: the capillary number Ca, denoting the ratio of viscous force of fluid flow to elastic interfacial force of MP, and the adhesion number Ad, representing the ratio of adhesion strength to viscous force of fluid flow. We systematically vary them numerically and a margination probability contour is obtained. We find that there exist two optimal regimes favoring high margination probability on the plane $Ca - Ad$. The first regime, namely region I, is that with high adhesion strength and moderate particle stiffness, and the other one, region II, has moderate adhesion strength and large particle stiffness. We conclude that the existence of optimal regimes is governed by the interplay of particle deformability and adhesion strength. The corresponding underlying mechanism is also discussed in detail. There are three major factors to contribute to the localization of MPs: (i) near-wall hydrodynamic collision between RBCs and MPs; (ii) deformation induced migration due to the presence of wall; (iii) adhesive interaction between MPs and the wall. (i) and (iii) promote margination, while (ii) hampers margination. These three factors perform different roles and compete against each other when MPs are located in different regions of the flow channel, i.e. near-wall region. In optimal region I, adhesion outperforms deformation induced migration, and in region II, the deformation induced migration is small compared to the coupling of near-wall hydrodynamic collision and adhesion. The finding of optimal regimes can help understand localization of elastic MPs at wall under the adhesion effect in blood flow. More importantly, our results suggest that softer MP or stronger adhesion is not always the best choice for the localization of MPs.

Key words: Elastic micro-particles, adhesion, margination, hydrodynamic collision, deformation induced migration

† Email address for correspondence: yingli@engr.uconn.edu

1. Introduction

Margination, defined as migration of a particle in blood flow towards the periphery of the blood vessel, allows the particle to come close to the endothelium, and then adhere to the vessel wall (marquis Du Trochet 1824; Koumoutsakos et al. 2013). It is of significant importance to understand such physiological processes for curing relevant diseases. For example, in inflammation process, margination of leukocytes towards the vessel wall is the precondition for organism to perform defense functions, such as adhering to vascular endothelium and transmigrating into the tissues (Ley & Tedder 1995; Fedosov et al. 2012). In atherosclerosis, the thrombosis, formed by the clot, is caused by the margination and accumulation of numerous platelets responding quickly to events on the vessel wall (e.g., injury) (Wootton & Ku 1999; Fogelson & Neeves 2015). Additionally, margination has extensive applications in microfluidic devices for the removal of pathogens and separation of cells (Hou et al. 2010; Gossett et al. 2010; Bhagat et al. 2010).

The root cause of margination has not been completely revealed so far. In the blood flow, every component of blood such as plasma and red blood cells (RBCs) may contribute to margination (Farutin & Misbah 2013). Generally speaking, three major factors: hydrodynamic forces, wall effects and adhesive interactions between ligands and receptors are considered to be responsible for the margination of micro-particles (MPs). Here, another most important effect, Brownian interaction in nano-particles, can be ignored due to the large size of MPs (Ramakrishnan et al. 2017). Hence, when placing the MP in the blood flow through injection or other administration, the dynamics of MPs is governed by the complex interplay among these three factors. The performance of the MP will be affected by its physiological properties such as size, shape, stiffness and surface functionality (also known as the '4S' parameters) (Li et al. 2016; Ye et al. 2018c). These properties play different roles, depending on the specific physiological conditions. For example, Decuzzi et al. (2010) found that in the in vivo experiment, discoidal particles demonstrated strongest accumulation in most of the organs such as spleen and kidney. While in the liver, cylindrical particles outperformed the other kinds of particles. Therefore, investigations of the '4S' parameters become crucial in the optimal design of MPs acting as drug carriers in biomedical application.

Among the '4S' parameters, stiffness attracts relatively less attention compared to other parameters. While it should play an important role in the margination process of MPs. Due to the deformability, the symmetry of the Stokes flow is broken. According to the mirror symmetry time reversal theorem proposed by Bretherton (1962), the elastic MP will experience a lateral force in the near wall region. For example, usually the leukocyte is assumed to marginate towards the vessel wall in blood flow (Fedosov et al. 2012; Freund 2007; Marth et al. 2016). Recently it has been discovered that the reversal of margination (migration from the near wall region to center of vessel) happens, when the stiffness is reduced by reorganization of cellular cortical actins (Fay et al. 2016).

The dynamics of elastic particle is more complex than rigid one. The shape of elastic MP is not given a priori and continuously deforms in flow. The evolution of shape is determined by the dynamic balance between the interfacial force and fluid stress, depending on the local flow environment. Additionally, a large number of RBCs occupies the blood flow. Thus, the deformation and moving of RBCs influence the flow field around MPs. Hydrodynamic interaction can also happen between RBCs and elastic MPs. Poiseuille (1836) recognized that blood corpuscles in the capillaries tended to migrate away from the

wall due to deformation induced migration stemming from viscous effects. Nevertheless, this stiffness dependent migration of particle attracts extensive attention very recently. Owing to the similar behavior of RBCs under flow, a series of elastic particles, such as capsules and vesicles, has been investigated in regards to their migration motion by experimental (Abkarian et al. 2002; Coupier et al. 2008; Kantsler et al. 2008; Callens et al. 2008), analytical (Olla 1997a,b; Qi & Shaqfeh 2017; Vlahovska & Gracia 2007; Seifert 1999; Danker et al. 2009; Farutin & Misbah 2011, 2013), and numerical studies (Cantat & Misbah 1999; Sukumaran & Seifert 2001; Secomb et al. 2007; Kaoui et al. 2008; Doddi & Bagchi 2008; Nix et al. 2014; Zhao et al. 2011; Singh et al. 2014). Quantitative determination of the deformation induced migration is instrumental to revealing the underlying mechanism of the migration behaviors of erythrocytes and leukocytes in the blood flow. Abkarian et al. (2002) used light microscopy to study the tank-treading motion and deformation of vesicles in linear shear flow. Upon increasing the shear rate of flow, the vesicle tilted with respect to the substrate, and further incrementation of shear rate $\dot{\gamma}$ made vesicle migrate away from substrate. These observations revealed the existence of deformation induced migration. They found that the magnitude of the deformation induced migration depended on the viscosity η of the fluid, the radius R of the vesicle, the distance h from the substrate, and a monotonous decreasing function $f(1-v)$ of the reduced volume v. On the basis of these direct observations, Farutin & Misbah (2013) derived the migration velocity of a vesicle near the wall. From the method using stresslet of droplet in Couette device (Smart & Leighton Jr 1991), they employed asymptotic method to derive the expression of migration velocity by determining stresslet in a power series of shape parameter Γ of vesicles. Γ quantifies the deflation of vesicle from sphere with the same volume. In the leading order of Γ, the migration velocity $\sim \dot{\gamma}R^3/h^2$. While the theoretical analysis was implemented on the basis of assumption that the deflation Γ is small. It means that if the shear modulus of the particles, such as that of the capsule, is not high, the expression should not be valid. More recently, Singh et al. (2014) corrected the analytical migration velocity by fitting the results obtained from a series of numerical simulations for capsules with different elastic capillary numbers Ca. They found that there existed a critical Ca_{cr} splitting the migration velocity into two distinct regimes. When $Ca < Ca_{cr}$, migration velocity $\sim Ca$ and $\sim \dot{\gamma}R^3/h^2$, which is similar to the analytical relation for vesicles. While when $Ca > Ca_{cr}$, migration velocity $\sim Ca^{0.6}$ and $\sim \dot{\gamma}R^{2.35}/h^{1.35}$. Hence, if the capsule is soft (large Ca), the analytic relation is not valid for the capsule any more. Also, a detailed study for lift velocity of RBC through simulations has been proposed by Qi & Shaqfeh (2017). Here, the elastic MPs pertain to capsules, and will be discussed in detail later.

According to Farutin & Misbah (2013), in addition to deformation induced migration, hydrodynamic interaction is an additional governing mechanism of particle migration in simple shear flow. Hydrodynamic interaction results in hydrodynamic diffusion, which is induced by collisions between particles. Collision between two identical particles, namely homogeneous collision such as capsules (Singh & Sarkar 2015) and vesicles (Farutin & Misbah 2013) are investigated numerically and theoretically, respectively. This homogeneous collision is not essential in particles migration and segregation, because the migrations of two collision parts are the same. Kumar & Graham (2011, 2012b) and Sinha & Graham (2016) extended this to heterogeneous collision between capsules with the same volume, but different membrane rigidities and shapes, respectively. In the binary suspension of soft and stiff capsules, the stiff particles were observed to accumulate in the near wall region in the suspension of primarily soft particles. While soft particles were found to concentrate on the centerline in the suspension of primarily stiff particles. This segregation behavior was attributed to larger cross-stream displacement in heterogeneous

collisions of stiff particle than that of soft particles. Furthermore, Vahidkhah & Bagchi (2015) proposed that binary collision between RBC and rigid MP should be one of the reasons for the shape dependent margination behaviors of MPs. The result presented that spherical and oblate MPs marginated more than prolate MPs after several collisions. In terms of the elastic MPs, the collision between MPs and RBCs will be more complex, and it should play an important role in margination behavior of elastic MPs. However, it remains largely unexplored so far.

After the particle marginates, it has a chance to interact with the vessel wall and adhere to it, depending on the ligand-receptor binding properties. Adhesion behavior has been extensively studied using the Bell model (Bell 1978), developed by adhesive dynamics which was first employed to understand the dynamics of leukocyte adhesion under flow (King & Hammer 2001; Hammer & Lauffenburger 1987; Hammer 2014). A number of studies in drug delivery systems focus on the adhesion process (Charoenphol et al. 2010, 2012; Decuzzi & Ferrari 2006; Coclite et al. 2017; Fedosov 2010; Luo & Bai 2016). In human blood, MPs with diameters of 3 μm were found to be the ideal choice for spherical, rigid particles to adhere to vessel walls rather than nano-particles (Charoenphol et al. 2010, 2012). In addition to spherical particles, Decuzzi & Ferrari (2006) investigated the effects of particle size and shape on the adhesion behavior from the point of specific adhesive interaction strength. They predicted that for a fixed shape (e.g., spherical or ellipsoidal), there existed an optimal volume (size) making the adhesive strength reach a maximum. Additionally, they found that non-spherical particles can carry a larger amount of drugs than spherical particles with the same adhesive strength. More recently, Coclite et al. (2017) constructed two-dimensional Lattice Boltzmann-immersed boundary model to systematically predict the near-wall dynamics of circulating particles with different shapes and adhesive strengths. As for adhesion behavior of deformable particles, a variety of dynamic phenomena, including detachment, rolling, firm adhesion and stop-and-go motion (Fedosov 2010; Luo & Bai 2016), were found. Luo & Bai (2016) combined front-tracking-finite element method and adhesion kinetics model to investigate capsule dynamics in flow and adhesive dynamics, respectively. It was found that, for the particle with low Ca, deformation promoted the rolling-to-firm adhesion transition. While the deformation would inhibit both rolling-to-firm adhesion and detachment-to-rolling transition when the Ca of the particle was relatively high. Because the particle with high Ca would collapse on the substrate, and in the middle of the particle, a ligand-receptor free region formed. Further increment of Ca made the rolling motion vanish and the particle shape largely deviate from spherical one.

In general, margination is thought to be the necessary precondition for the adhesion (Müller et al. 2016). Before particle can interact with vessel wall, it should marginate into near wall region, e.g. cell-free layer (CFL) in the blood flow. The CFL is a thin layer near vessel wall with no RBCs inside, which forms due to the deformability of RBCs. However, adhesion can also, in turn, affect the margination process. In engineering applications, micron-sized particles are often used as drug carriers due to their better performance over nano-sized particles in the margination process (Tasciotti et al. 2008). The thickness of the CFL is also measured in micron-size (about $1.5 \sim 5.0$ μm) in human vasculature (Fedosov et al. 2010b). Hence, when particle moves close to or enters the CFL, the particle can interact with vessel wall through ligand-receptor binding. Additionally, in terms of deformation of particle, the elastic MP may move away from wall to center of blood flow due to deformation induced migration. But adhesion may play a role in preventing it escaping from the CFL. Thus, the adhesion will affect the choice of elastic MP located near the CFL: entering or departing from the CFL? Such phenomenon was also reported in previous work (Müller et al. 2016), but without discussion. Researchers

pay more attentions to effects of particle '4S' properties on either margination or adhesion (Vahidkhah & Bagchi 2015; Decuzzi & Ferrari 2006; Müller et al. 2014).

Considering above aspects, we focus on the performance of elastic MPs in the whole process from margination to adhesion. We combine Lattice Boltzmann Method and molecular dynamics to solve fluid dynamics and particles (RBCs and elastic MPs) dynamics, respectively. These two parts are coupled by immersed boundary method. In our simulation, the most expensive part is solving of fluid dynamics. The LBM is adopted due to its high natural parallelism. In the past two decades, it has been confirmed as an efficient and accurate numerical solver to handle fluid dynamics problems (Higuera et al. 1989; Benzi et al. 1992; Chen & Doolen 1998). Its application in simulating blood flow acquires significant progress (Aidun & Clausen 2010; Zhang et al. 2007, 2008; Macmeccan et al. 2009; Clausen et al. 2010; Melchionna et al. 2010; Lorenz et al. 2009; de Haan et al. 2018; Czaja et al. 2018). In the absence of large numbers of RBCs, Melchionna et al. (2010) took a hydrokinetic approach (Bernaschi et al. 2009) to model large scale cardiovascular blood flow to recognize the key relevance to the localization and progression of major cardiovascular diseases, such as atherosclerosis. Borgdorff et al. (2014) provided a multiscale coupling library and environment to make the simulation of extra large scale vasculature network become doable. Furthermore, considering the existence of RBCs, Zhang et al. (2008, 2007) conducted simulations from aggregation of multiple RBCs to rheology of RBC suspension in two dimensional blood flow. Macmeccan et al. (2009) and Clausen et al. (2010) extended it to three dimensional blood flow by coupling LBM with finite element method. Additionally, adhesive dynamics of elastic MPs to vessel wall is governed by the probabilistic model proposed by Hammer & Lauffenburger (1987). The diameter of MPs are set as 2 μm, and the hematocrit of blood flow is 30%, in which the thickness of CFL is comparable to the particle size. To clarify the influence of near wall adhesion on localization of MPs, the particle size and blood flow conditions are fixed. The Ca is tuned by changing shear modulus of elastic MPs, and we vary the adhesion strength to adjust the Ad. The interplay of adhesion strength and particle deformability leads to two optimal margination regimes. One is with moderate Ca and high Ad, and the other is with small Ca and moderate Ad. This may shed light on the optimal design of MPs favoring high localization at wall in blood flow.

The paper is organized as follows. Section 2 describes the physical problem involving elastic MPs transport in blood flow and numerical methods we employ to solve fluid flow, particle dynamics and adhesive dynamics. We validate our computational method in Section 3. Furthermore, Section 4 presents the margination and adhesion results. A detailed discussion of underlying physical mechanisms is also provided. In section 5, conclusions are given.

2. Physical Problem and Computational Method

2.1. Physical problem

In the blood flow, most parts of the vessel are occupied by a large number of RBCs. In the normal human blood vessel, the volume fraction (hematocrit Ht) is about $20 \sim 45\%$. Under the interplay effect of the flow and vessel wall, RBCs move from the near wall region to the center of vessel due to deformation induced migration. It results in the formation of a cell-free layer (CFL). The CFL plays a role as a lubricant layer and reduces the blood flow resistance, which is also called Fahraeus-Lindqvist effect (Fåhræus & Lindqvist 1931). When the elastic MPs, acting as drug carriers, are injected into a

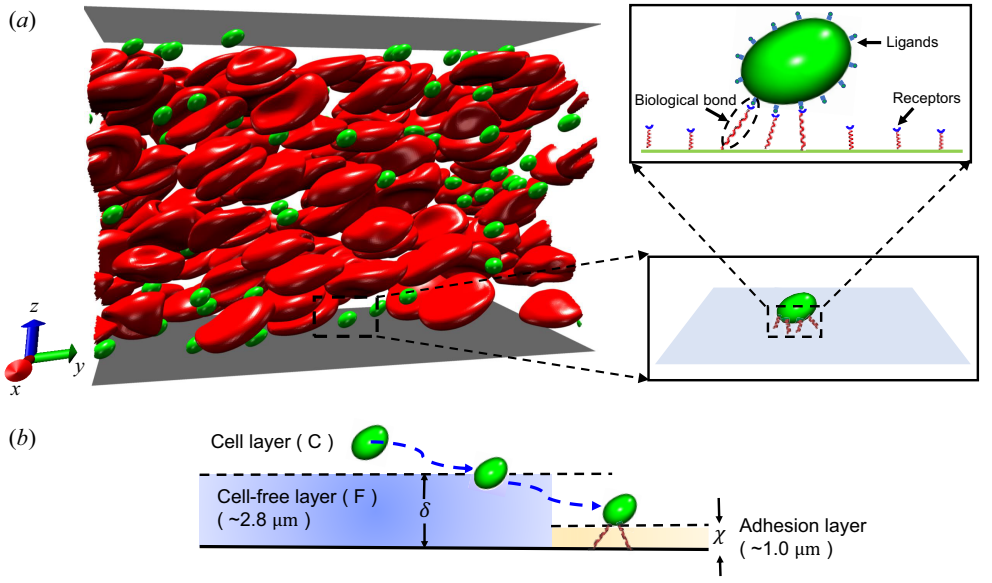

Figure 1. Transport of elastic MPs in blood flow. (a) Computational model of margination and adhesion of elastic MPs in blood flow. Zoom-in figures give the detailed adhesion behavior of elastic MP under stochastic ligand-receptor binding effect. (b) Schematic of transport process of elastic MP from center of blood stream (denoted as C) to cell-free layer (F), and then reaching adhesion layer.

vein, they move with bulk flow as shown in figure 1a. The elastic MPs deform under the shear stress and collide with RBCs. And the deformation depends on the local flow environment. Additionally, the MPs may move in the cross-stream direction, migrating either towards the wall or to the center of the channel. Once MPs migrate to the near wall region, i.e., CFL, the ligands decorated on their surfaces have the chance to interact with the receptors on the endothelial cell distributed on the vessel wall (figure 1a). And this ligand-receptor binding is required for the further release of drug molecules into tumor sites through vascular targeting strategy (Schnitzer 1998; Neri & Bicknell 2005). However, reaching the CFL cannot guarantee that such interactions will occur. Only when the MP reaches a closer distance to the vessel wall, in which ligands can interact with receptors, the interaction occurs. This distance is determined by the reaction distance between ligands and receptors. We name the layer within this distance as adhesion layer (χ). Usually the thickness of the adhesion layer is in the range of tens to hundreds nanometers (Decuzzi & Ferrari 2006; Müller et al. 2014, 2016). Here, it is set as 1.0 μm according to the reaction distance we used in the computational model. And it is reasonable compared to that in previous work of Müller et al. (2014).

The numerical study is employed to study the transport of elastic MPs due to its flexibility in tuning the properties of MPs and adhesive interactions. The blood flow is considered a suspension of RBCs. Limited to computation resource, a small part of the vessel is taken into account and modeled as a rectangular channel. The size of the channel is of height 36 μm, width 27 μm and length 54 μm. Periodical boundary conditions are applied in width (x) and length (y) directions. Height (z) direction is bounded by two flat plates. The bottom plate (vessel wall, also namely substrate) is fixed and the flow is driven by the moving of upper one with a constant velocity U. In all of the simulations, shear rates stay at 200 s^{-1}. 162 RBCs and 80 identical elastic MPs are placed inside the channel. The hematocrit (volume fraction of RBCs) is about 30%. MPs are initially set

Parameters	Simulation	Physical Value
Equilibrium length of bond (l_0)	1	250 nm
Bond strength (k_s)	$2.6\times10^{-5}\sim1.2\times10^{-2}$	$1.64\times10^{-9}\sim7.56\times10^{-6}$ N/m
Reactive and rupture distance (d_{on} and d_{off})	4	$1\mu m$
On strength (σ_{on})	0.7305	1.9×10^{-7} N/m
Off strength (σ_{off})	0.7305	1.9×10^{-7} N/m
Unstressed on rate (k^0_{on})	3.75	1.3×10^{6} s^{-1}
Unstressed off rate (k^0_{off})	0.05	1.8×10^{4} s^{-1}
Ligand density (n_l)	4.11	66 $mol/\mu m^2$
Receptor density (n_r)	1.0	16 $mol/\mu m^2$

Table 1. Parameters used in adhesive model for ligand-receptor binding.

to spherical shape with radius 1 μm, and their total volume fraction is about 0.64% in the channel. Additionally, on the surfaces of MPs and substrate, the ligands and receptors are uniformly distributed, respectively. The densities of ligands and receptors are listed in Table 1.

2.2. Computational method

2.2.1. Lattice Boltzmann method for fluid flow

The RBCs are immersed within blood plasma in the blood flow. The other components, such as the white blood cells and platelets are negligible due to their low volume fractions compared to that of RBCs. The plasma is usually considered as a Newtonian fluid. And its dynamics is described by the continuity equation and incompressible Navier-Stokes (NS) equation:

$$\nabla\cdot\mathrm{u}=0, \tag{2.1}$$

$$\rho\frac{\partial\mathrm{u}}{\partial t}+\rho\mathrm{u}\cdot\nabla\mathrm{u}=-\nabla p+\mu\nabla^2\mathrm{u}+\mathrm{F}, \tag{2.2}$$

where ρ is the plasma density, u and p represent the velocity and pressure of the flow, respectively. The term F on the right-hand side of Eq. (2.2) is the external force. μ is the dynamic viscosity of the plasma and it is set as 1.2 cP. The Lattice Boltzmann (LB) method is employed to solve the NS equation due to its high efficiency and accuracy to handle incompressible Newtonian flow (Higuera et al. 1989; Benzi et al. 1992; Chen & Doolen 1998). By discretizing velocity of the linearized Boltzmann equation, a finite difference scheme is obtained:

$$f_i(\mathrm{x}+\mathrm{e}_i\Delta t,t+\Delta t)=f_i(\mathrm{x},t)-\frac{\Delta t}{\tau}(f_i-f_i^{eq})+F_i, \tag{2.3}$$

where $f_i(\mathrm{x},t)$ is distribution function and e_i is the discretized velocity. In the current simulation, the D3Q19 velocity model is used (Mackay et al. 2013), and the fluid particles have possible discrete velocities stated in Mackay et al. (2013). τ denotes the non-dimensional relaxation time, which is related to the dynamic viscosity in NS equation as the form:

$$\mu=\rho c_s^2(\tau-\frac{1}{2})\Delta t. \tag{2.4}$$

$f_i^{eq}(\mathrm{x},t)$ is the equilibrium distribution function and F_i is the discretized scheme of external force. In current simulation, the equilibrium distribution function adopts the

form:

$$f_i^{eq}(\mathbf{x},t) = \omega_i \rho \left[1 + \frac{\mathbf{e}_i \cdot \mathbf{u}}{c_s^2} + \frac{(\mathbf{e}_i \cdot \mathbf{u})^2}{2c_s^4} - \frac{(\mathbf{u})^2}{2c_s^2}\right], \tag{2.5}$$

where the weighting coefficients $\omega_i = 1/3$ $(i = 0), \omega_i = 1/18$ $(i = 1-6), \omega_i = 1/36$ $(i = 7-18)$. The term c_s represents the sound speed which equals $\Delta x/(\sqrt{3}\Delta t)$. The external forcing term can be discretized by the form (Guo et al. 2002):

$$F_i = (1 - \frac{1}{2\tau})\omega_i \left[\frac{\mathrm{e}_i - \mathrm{u}}{c_s^2} + \frac{(\mathrm{e}_i \cdot \mathrm{u})}{c_s^4}\mathrm{e}_i\right] \cdot \mathrm{F}. \tag{2.6}$$

Eq. (2.3) is advanced through the algorithm proposed by Ollila et al. (2011). Here, the solver of LB is embedded in Large-scale Atomic/Molecular Massively Parallel Simulator (LAMMPS) (Plimpton 1995), which is implemented by Mackay et al. (2013). After the particle density distributions are known in the whole fluid domain, the properties of fluid, such as fluid density and velocity can be calculated as:

$$\rho = \sum_i f_i, \ \mathbf{u} = \frac{1}{\rho}\sum_i f_i \mathbf{e}_i + \frac{1}{2\rho}\mathrm{F}\Delta t. \tag{2.7}$$

2.2.2. Coarse-grained models for RBC and MP

To capture the dynamics and deformation of RBCs and elastic MPs, we develop a coarse-grained model and implement it into LAMMPS (Ye et al. 2018b). The RBC is modeled as liquid-filled coarse-grained membrane, and its equilibrium shape is biconcave. The diameter of a RBC is 7.8 μm, and the thickness is about 2.1 μm. The surface area and volume of RBC are 134.1 μm^2 and 94.1 μm^3, respectively (Evans & Skalak 1980). In the simulation, the membrane is discretized into 3286 vertices and 6568 triangular elements.

To capture the in-plane shear property of RBC, a stretching potential $U_{stretching}$ is used. It includes two parts: attractive nonlinear spring potential - wormlike chain model (WLC) and repulsive power potential - power function (POW) (Fedosov et al. 2010a, 2011b). They can be expressed as:

$$U_{WLC} = \frac{k_\mathrm{B} T l_m}{4p}\frac{3x^2 - 2x^3}{1-x}, \ U_{POW} = \frac{k_p}{l}, \tag{2.8}$$

where $k_\mathrm{B}T$ is the basic energy unit. $x = l/l_m \in (0,1)$, l is the length of the spring and l_m is the maximum spring extension. p is the persistent length, and k_p is the POW force coefficient. Applying bending potential

$$U_{bending} = \sum_{k \in 1...N_s} k_b[1 - \cos(\theta_k - \theta_0)], \tag{2.9}$$

the out-of-plane bending property of RBC is reflected. k_b is the bending stiffness. θ_k is dihedral angle between two adjacent triangular elements, and θ_0 is the initial value of dihedral angle. In the following, subscript 0 represents the corresponding initial value. N_s denotes the total number of dihedral angles.

Besides, the bulk properties, such as surface area and volume conservation are ensured by introducing the penalty forms:

$$U_{area} = \sum_{k=1...N_t} \frac{k_d(A_k - A_{k0})^2}{2A_{k0}} + \frac{k_a(A_t - A_{t0})^2}{2A_t}, \tag{2.10}$$

and

$$U_{volume} = \frac{k_v(V - V_0)}{2V_0}, \tag{2.11}$$

where the first term in Eq. (2.10) represents the local area constraint, A_k and A_{k0} denote the area of k-th element and its initial area, respectively, and k_d is the corresponding spring constant. The second term in Eq. (2.10) is the global area constraint. A_t is the total area, and k_a is the spring constant. In Eq. (2.11), k_v is the spring constant and V is total volume.

Then the total energy U is:

$$U = U_{WLC} + U_{POW} + U_{bending} + U_{area} + U_{volume}. \tag{2.12}$$

The nodal forces exerted on each vertexes of the RBC membrane are derived by:

$$f_i = -\partial U(X_i)/\partial X_i, \tag{2.13}$$

where X_i denotes the vertex of RBC membrane. Thus, if we know the position of membrane vertexes, we can calculate the nodal force according to Eq. (2.13). The detailed derivation of the force formulae such as two-point stretching force and three-point bending force are presented in Ye et al. (2018b).

The elastic MPs adopt the same model as RBCs, but with 828 vertices and changeable in-plane shear strength. Before we choose the parameters for the coarse-grained model of RBCs and elastic MPs, we should know the corresponding macroscopic properties through experiments as a priori. According to the relationship between coarse-grained model parameters and macroscopic properties (Allen & Tildesley 1989; Dao et al. 2006; Fedosov et al. 2010a)

$$\begin{aligned} \mu_0 &= \frac{\sqrt{3}k_BT}{4pl_mx_0}\left(\frac{x_0}{2(1-x_0)^3} - \frac{1}{4(1-x_0)^2} + \frac{1}{4}\right) + \frac{3\sqrt{3}k_p}{4l_0^3}, \\ K &= 2\mu_0 + k_a + k_d, \\ Y &= \frac{4K\mu_0}{K + \mu_0}, \end{aligned} \tag{2.14}$$

where μ_0 is the shear modulus, K represents the area compression modulus and Y denotes the Young's modulus. Therefore, the potential parameters can be chosen on the basis of the physical quantities. The parameters used in the simulation are listed in Table. 2.

The accuracy of this model for RBC and elastic MP has been validated in our previous works (Ye et al. 2018a,b, 2017a). In Section 3, we will show two more validations to confirm the convergence of both fluid and membrane meshes and modeling of rheology of blood flow. The details about the computational efficiency and cost are discussed in Section 5 and Ye et al. (2018b). In addition to the above potentials, it is necessary to employ inter-molecular interactions between RBCs to characterize their interactions. Here we use the Morse potential as inter-molecular interactions (Liu & Liu 2006; Fedosov et al. 2011b; Tan et al. 2012), with the form

$$U_{morse} = D_0[e^{-2\beta(r-r_0)} - 2e^{-\beta(r-r_0)}], r < r_c, \tag{2.15}$$

where D_0 represents the energy well depth and β controls the width of potential well, r is the distance between two particles and r_0 is the equilibrium distance, r_c is the cutoff distance. Additionally, a short range and pure repulsive Lennard-Jones potential is applied to prevent the overlap between RBCs and MPs (Ye et al. 2018b).

Parameters	Simulation	Physical Value
RBC diameter (D_r)	32	$8\times10^{-6}\ m$
MP diameter ($2R$)	8	$2\times10^{-6}\ m$
RBC shear modulus (μ_r)	0.01	$6.3\times10^{-6}\ N/m$
MP shear modulus (μ_0)	$10^{-4}\sim1.0$	$6.3\times10^{-8}\sim6.3\times10^{-4}\ N/m$
Energy scale (k_BT)	1.1×10^{-4}	$4.14\times10^{-21}\ N\cdot m$
Viscosity of fluid (η)	0.167	$0.0012\ Pa\cdot s$
Area constant (k_a)	0.0075	$4.72\times10^{-6}\ N/m$
Local area constant (k_d)	0.367	$2.31\times10^{-4}\ N/m$
Volume constant (k_v)	0.096	$249\ N/m^2$
RBC bending constant (k_b)	0.013	$5\times10^{-19}\ N\cdot m$

Table 2. Coarse-grained potential parameters for red blood cells and elastic MPs, and their corresponding physical values.

2.2.3. Immersed boundary method for fluid-structure interaction

The immersed boundary (IB) method is used to couple LBM with LAMMPS to account for fluid-structure interaction (Peskin 2002; Krüger et al. 2011, 2014; Ye et al. 2017b). We use the Lagrangian (X) and Eulerian (x) mesh points in the computational domain to represent RBC (or MP) and fluid particles, respectively. The Eulerian fluid mesh is uniform and the resolution is $\Delta x = 250\ nm$ in all directions. The Lagrangian mesh for RBC or MP is generated by MATLAB code (Persson & Strang 2004; Persson 2005). The mesh is approximately uniform and the mesh size is set about $\Delta X = 0.6\sim0.8\Delta x$. Then there are about 32 Eulerian points across one RBC in diametral direction. It is sufficient to resolute the deformation and motion of RBC (Macmeccan et al. 2009; Vahidkhah & Bagchi 2015). The coupling is fulfilled by the interpolation of velocity and force distribution between Lagrangian and Eulerian mesh points (Mittal & Iaccarino 2005).

To ensure no-slip boundary condition, the membrane vertices X with Lagrangian coordinate s should move at the same velocity as the fluid around it. That is

$$\frac{\partial \mathrm{X}(s,t)}{\partial t} = \mathrm{u}(\mathrm{X}(s,t)). \tag{2.16}$$

The velocity can be interpolated by the fluid velocity through a smoothed Dirac-Delta function δ:

$$\mathrm{u}(\mathrm{X},t) = \int_\Omega \mathrm{u}(\mathrm{x},t)\delta(\mathrm{x}-\mathrm{x}(\mathrm{X},t))d\Omega. \tag{2.17}$$

This condition will cause the membrane to move and deform. The membrane force density $\mathrm{F}(s,t)$ is obtained by derivation of potential functions as Eq. (2.13), and is distributed to the surrounding fluid mesh points by

$$\mathrm{f}^{fsi}(\mathrm{x},t) = \int_\Omega \mathrm{F}^{fsi}(\mathrm{X},t)\delta(\mathrm{x}-\mathrm{x}(\mathrm{X},t))d\Omega. \tag{2.18}$$

2.2.4. Adhesive model for ligand-receptor binding

The ligand-receptor binding is described by the association and dissociation of biological bonds. And it is governed by the probabilistic adhesion model (Hammer & Lauffenburger 1987). Figure 1(a) gives the schematic of the adhesive model. When the ligands on the MP approach the receptors on the vessel wall, they have the chance to bind together. And it is determined by the probability P_{on}. Reversely, the existing bond

has a probability P_{off} to break. They can be expressed as:

$$P_{on} = \begin{cases} 1 - e^{-k_{on}\Delta t}, & l < d_{on} \\ 0, & l \geqslant d_{on} \end{cases}, \quad P_{off} = \begin{cases} 1 - e^{-k_{off}\Delta t}, & l < d_{off} \\ 0, & l \geqslant d_{off} \end{cases}, \tag{2.19}$$

where Δt is the time step in simulation, d_{on} and d_{off} are the cutoffs for bond creation and breakup, respectively. k_{on} and k_{off} are the association and dissociation rates with the forms:

$$k_{on} = k_{on}^0 exp(-\frac{\sigma_{on}(l-l_0)^2}{2k_BT}), \quad k_{off} = k_{off}^0 exp(\frac{\sigma_{off}(l-l_0)^2}{2k_BT}), \tag{2.20}$$

where σ_{on} and σ_{off} are the effective on and off strengths, representing a decrease and increase of the corresponding rates within d_{on} and d_{off}, respectively. k_{on}^0 and k_{off}^0 are the reaction rates at the equilibrium length $l = l_0$ between ligand and receptor. The mechanical property of biological bond is described by a harmonic spring. l_0 is the equilibrium length, and the force exerted on the receptor and ligand is: $F_b = k_s(l - l_0)$. Here, k_s represents the adhesive strength. This model and the relevant parameters (c.f. Table. 1) are chosen according to previous works of Fedosov (2010) and Fedosov et al. (2011a).

There are three dimensionless parameters, including

$$\text{Reynolds number}: \quad \mathrm{Re} = \rho\dot{\gamma}\mathrm{R}^2/\mu, \tag{2.21}$$

$$\text{Capillary number}: \quad \mathrm{Ca} = \mu\dot{\gamma}\mathrm{R}/\mu_0, \tag{2.22}$$

$$\text{Adhesion number}: \quad \mathrm{Ad} = \mathrm{k_s}/\mu\dot{\gamma}\mathrm{R}. \tag{2.23}$$

Considering the physiological environment surrounding the cell, the fluid flow is considered as a Stokes flow. Thus, Re is very small, and we fix its value $Re = 0.0134$ to approximately represent the Stokes regime. The capillary number represents the ratio of shear stress exerted on the surface of elastic MP to elastic force induced by deformation of elastic MP. μ_0 is the shear modulus of the MP. The higher the Ca, the softer of the particle. The adhesion number denotes the ratio of adhesive strength to shear stress of flow. Thus, the higher the Ad, the stronger the adhesion strength. In our simulations, Ca is tuned by varying shear modulus μ_0, and Ad is varied by changing adhesive strength k_s.

3. Validation of Numerical Method

The grid independence studies of fluid and RBC membrane are conducted. We perform a case study that a single RBC with diameter (D_r) moves in simple shear flow ($v(z) = \dot{\gamma}z$) shown in figure 2(a). Here the RBC is discretized with different vertexes presented in figure 2(b). To exclude the size effect of the channel, we adopt the same channel and same shear rate as the margination studies of MPs. First, we vary the mesh size Δx of the fluid, and track the trajectories of the center of RBC in height direction (z-direction). Figure 2(c) shows that when the mesh is coarse ($\Delta x = 1/8D_r$), the trajectory is obviously different from those with fine meshes, and it is not smooth compared to those with fine meshes. Further increase of mesh resolution ($\Delta x = 1/16D_r$) leads to a more consistent trajectory, and only small difference of trajectory exists between it and finer mesh. When the mesh resolution increases to $\Delta x = 1/32D_r$, the difference between it with the finer mesh can be negligible. Thus, current study adopts the mesh size $\Delta x = 1/32D_r$. Furthermore, we change the discretized vertexes of the RBC membrane. Four cases $V = 766, 1418, 3286$ and 9864 are investigated here. V and T represent the numbers of vertex and triangular

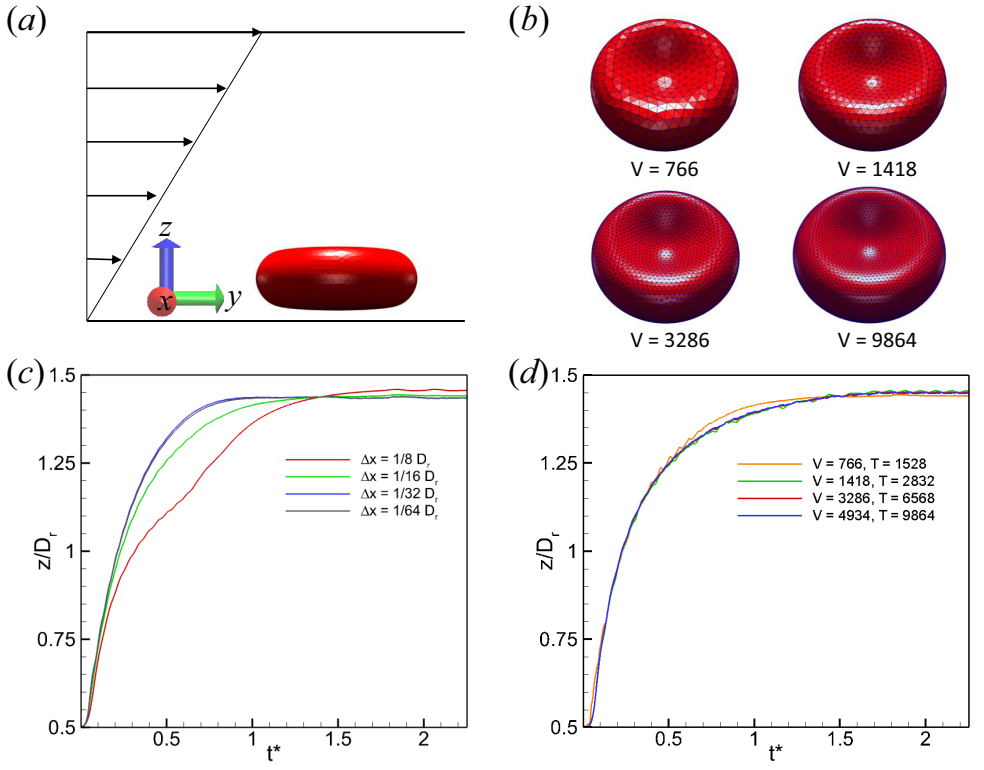

Figure 2. Grid independence studies. (a) Model of motion of single RBC in simple shear flow. (B) Discretization of RBC membrane with different vertexes. (c) Grid independence of fluid mesh. (d) Grid independence of RBC discretization.

element of RBC membrane, respectively. Again, we track the trajectories of the center of RBC in the height direction. We find that the discretization of the membrane has weak influence on the motion of RBC under current scheme ($766 < V < 9864$). There is only a small difference for the case of $V = 766$, comparing to other cases. To ensure enough convergence of membrane mesh, we adopt a relatively fine mesh $V = 3286$. In the following simulations, the fluid mesh size is $\Delta x = 1/32D_r$ and the discretization of RBC membrane is $V = 3286$.

Here, we conduct the Fahraeus effect and Fahraeus-Lindqvist effect of blood flow with different hematocrits (15% and 30%) in the tube with different diameters (10 μm, 20 μm and 40 μm) to validate our numerical method in terms of rheology of blood flow. The length of the tube is fixed as three times of the diameter.

The Fahraeus effect presented an increased value of discharge hematocrit (H_d) measured at the tube exit in comparison with that before the tube entrance. It was first discovered in in vitro experiments of blood flow in tube (Fåhraeus 1929). In our simulation, we take the same definition as that in Fedosov et al. (2010b) to calculate the discharge hematocrit.

$$H_d = \frac{\bar{v}_c}{\bar{v}} H_t, \tag{3.1}$$

where $\bar{v} = Q/A$ is the mean velocity of the blood flow, and $\bar{v}_c$ is the average cell velocity averaged in time in the steady-state regime.

The Fahraeus-Lindqvist effect stated that apparent blood viscosity decreased with

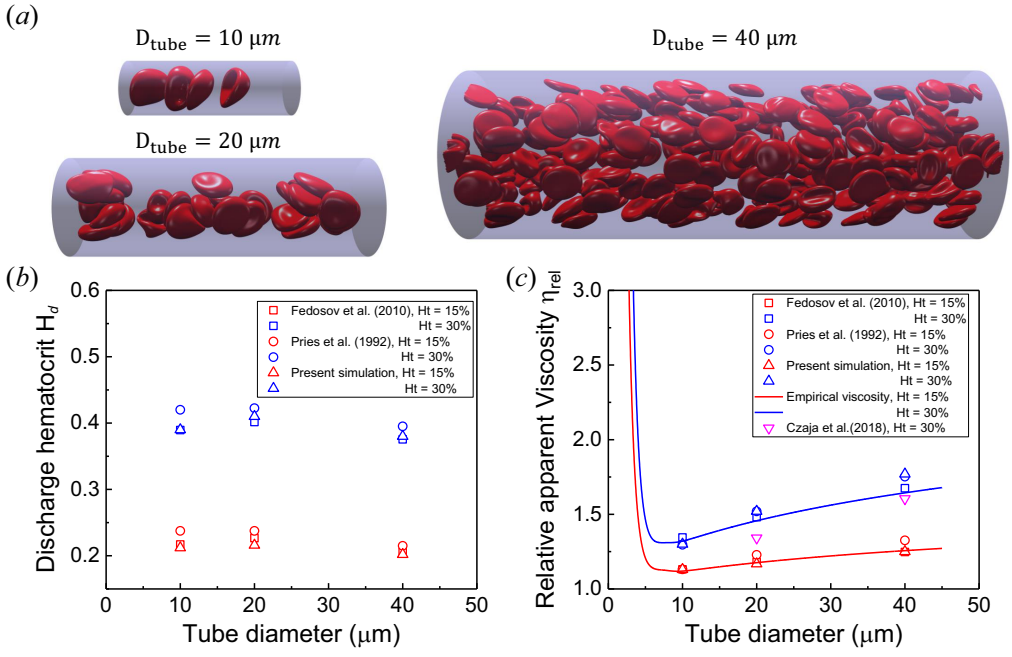

Figure 3. Fahraeus and Fahraeus-Lindqvist effects. (a) Snapshots to show the tube flow with different diameters under hematocrit 15%. (b) Fahraeus effect: discharge hematocrit comparison. (c) Fahraeus-Lindqvist effect: relative viscosity validation.

decrease of tube diameter found in experiments (Fåhræus & Lindqvist 1931; Pries et al. 1992, 1994). And it is usually convenient to calculate the relative apparent viscosity to investigate this effect, which is defined as:

$$\eta_{rel} = \frac{\eta_{apparent}}{\eta_{plasma}}, \tag{3.2}$$

where the apparent viscosity $\eta_{apparent} = \Delta P D_{tube}^2 / 32 \bar{v} L$. ΔP and L are pressure difference between inlet and outlet of the tube and length of the tube, respectively.

In figure 3(a), we show the snapshots of blood flow in tube with different diameters under hematocrit 15%. We calculate the discharge hematocrit and relative viscosity of the blood flow, and compare our results with those in experiment (Pries et al. 1992) and numerical (Fedosov et al. 2010b; Czaja et al. 2018) studies in figure 3(b) and (c). As for the relative viscosity of the blood flow, we also provide the empirical viscosity from experiment (Pries et al. 1994). We find that our results are more consistent with empirical value under low hematocrit 15% compared with that under hematocrit 30%. What's more, the results have a more consistence with the numerical results than that with empirical results. The discrepancies existed between numerical simulations and experiments may be induced by the interaction between RBC and tube wall, and estimation method in experiments (Fedosov et al. 2010b). However, current study has adequate accuracy to model the blood flow from above comparison.

4. Results and Discussion

We study the margination behaviors of elastic MPs (i) without ($Ad = 0$) and (ii) with ($Ad = 0.07 \sim 32.8$) adhesion. The stiffness of the elastic MPs is varied by changing the

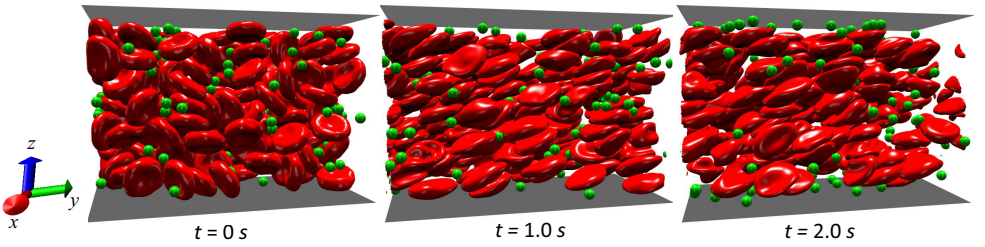

Figure 4. Snapshots to show the margination behavior of elastic MP ($Ca = 0.0037$) without effect of adhesion.

shear modulus μ_0, which makes Ca range from 0.00037 to 3.7. It corresponds to the shear modulus of MP from 6.3×10^{-4} to 6.3×10^{-8} N/m (note that shear modulus of RBC is 6.3×10^{-6} N/m). The elastic MPs are randomly placed among RBCs in the whole channel at the beginning of all simulations. For MPs with different shear moduli, they have the same initial configurations. It can eliminate the influence of initial condition on the margination results.

4.1. Margination of elastic MPs without adhesion

The margination of MPs without adhesion is first investigated. The margination process of a typical case of MPs with $Ca = 0.0037$ is shown in figure 4. In these snapshots, at $t = 0$ s, we can see that MPs are randomly distributed as well as RBCs. The RBCs and MPs are considered at their equilibrium states. The shapes of RBCs and MPs are biconcave and spherical, respectively. At time $t = 1.0$ s, the fluid flow is developed. A large deformation has been observed for RBCs. Under the shear flow, we find that RBCs align their major axes along the flow direction. Though the deformation of MPs is small due to their high stiffness (small $Ca = 0.0037$), it should deform under the shear stress. And the deformation will be significant for case with high Ca. In addition to the deformation, RBCs and MPs both demonstrate cross-stream migration, but towards the opposite directions. RBCs migrate from near wall region to the center of channel, while MPs move towards the wall. We also find that the CFL becomes clear and some MPs have reached the CFL quickly. As simulation time further advances, at $t = 2.0$ s, the CFL is fully developed and MPs start to accumulate at the CFL.

Localization of MPs at wall is characterized by margination probability $\Phi(t)$, which is defined as:

$$\Phi(t) = \frac{n_f(t)}{N}, \tag{4.1}$$

where $n_f(t)$ represents the number of MPs with centers locating in CFL at time t, and N denotes the total number of MPs in the channel. Before quantifying the margination probability, the thickness of CFL is estimated in the absence of MPs. We use the same method proposed by Fedosov et al. (2010b), the thickness of CFL is about 2.8 μm for current blood flow with $Ht = 30\%$. This is consistent with previous numerical studies (Lee et al. 2013; Müller et al. 2014). Figure 5(a) gives the evolution of margination probabilities Φ for three different stiffnesses ($Ca = 0.00037, 0.037$ and 3.7). We find that the margination process can be split into two stages. In the first stage, the margination probability increases very fast, which signifies that there are more and more particles moving from the center to CFL. We note that, in this stage, the margination probabilities of softer particles increase faster ($Ca = 0.037$ and 3.7) than that of stiff particles ($Ca = 0.00037$). However, the duration of this stage for stiff particles is longer than those of soft particles. Therefore, when the first stage ends, the margination probability of stiff

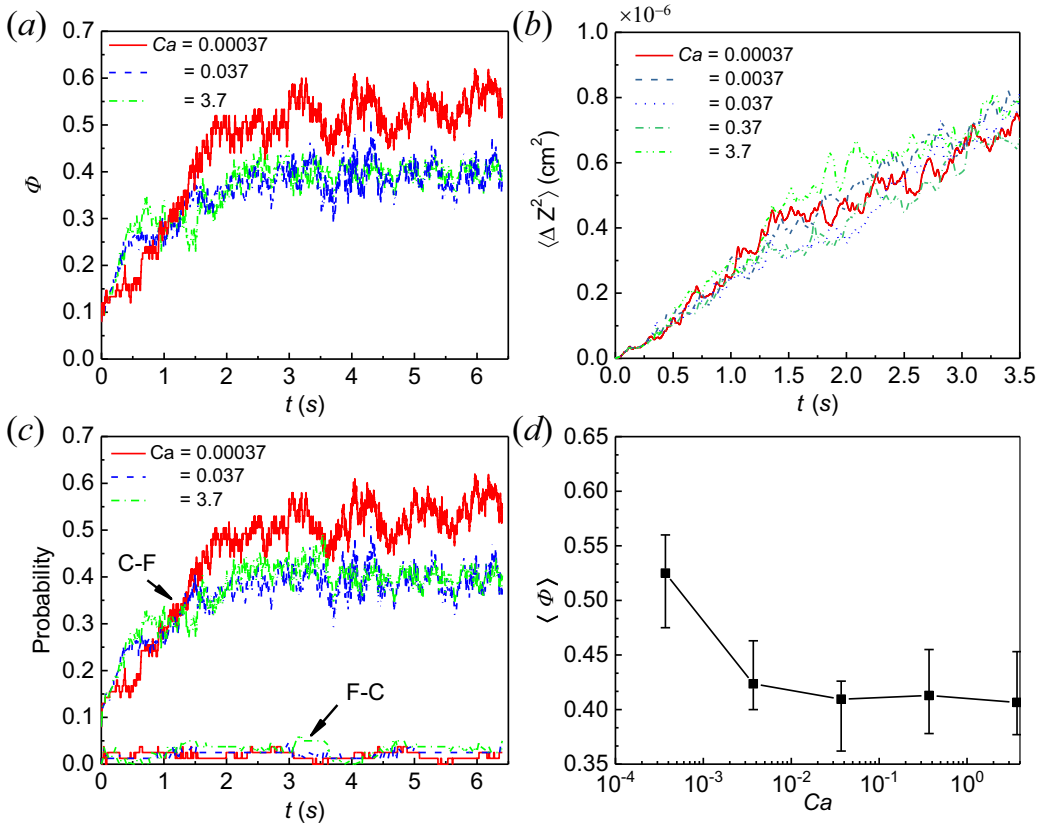

Figure 5. Margination behavior of elastic MPs with different stiffnesses. (a) Evolution of margination probabilities for elastic MPs. (b) Mean square displacement of elastic MPs during margination. (c) Probabilities of two types of motion: center to cell-free layer (C-F) and cell-free layer to center (F-C). (d) Time-averaged margination probability at steady-state regime.

particles is higher than those of soft ones. In the second stage, margination probabilities of both stiff and soft particles increase slower than those in the first stage. And the growth rates for these particles are almost the same.

To investigate this stiffness-dependency of margination behavior, the mean square displacements (MSDs) for MPs with different stiffnesses are calculated. The deformation of RBCs in the blood flow induces the fluctuation of flow around them. It is considered as the root cause of migration of rigid particles such as platelets in blood flow (Zhao et al. 2012). From figure 5(b), we find that there are no obvious difference among MSDs for all of the MPs. At the initial stage ($t < 1.0\ s$), the MSDs are almost the same. After that, the MSDs for MPs become different, but with only small variations. We calculate the diffusivities, defined as $D =< \Delta z^2 > /2t$, and they range from about 0.9 to $1.2 \times 10^{-7} cm^{-2} s^{-1}$ for these MPs. This is in good agreement with previous studies (Vahidkhah & Bagchi 2015; Zhao & Shaqfeh 2011). The diffusivity is about 2 orders of magnitude higher than the Brownian diffusivity, which means the existence of RBCs augments the diffusion of MPs. However, from these results, RBCs augmentation of diffusion is stiffness independent. Thus, the diffusion can not solely explain the observed stiffness-dependency of margination behavior.

To gain a better insight into the margination behavior, the motion types of MPs in blood flow are studied. Compared to rigid particles in blood flow, elastic MPs may

experience deformation induced migration, which can drive them to move away from the vessel wall (Kumar & Graham 2012b; Coupier et al. 2008). And this is the essential mechanism for CFL formation in blood vessel. Here the motion of elastic MPs can be classified into four types: (i) staying in the center; (ii) staying in the CFL; (iii) moving from center to CFL (C-F); and (iv) moving from CFL to the center (F-C). Obviously, the first two types cannot contribute to the localization of MPs at wall. The margination probability is attributed to the difference between the last two types as shown in figure 5(c). We find that the probabilities of F-C motion for all of the elastic MPs are the same and the values are almost 0. It indicates that there are only few particles migrating from CFL to the center region. We also observe that the C-F motion has the same tendency as the margination probability $\boldsymbol{\Phi}$. All these results lead to the conclusion that localization of MPs at wall in current study is determined by the C-F motion. This is different from our previous study in Ye et al. (2017a), in which F-C motion at some time can dominate the margination behavior of particles. The reason causing this difference mainly lies on the size of the particle and hematocrit of blood flow. If the size of the particle is large (2 μm in diameter), and the hematocrit is high (30%), there is no available space for the particle to stay in the center of the channel. Because, under shear flow, the most parts of center region are occupied by RBCs. Hence, F-C motion is not significant in present study.

To quantify the stiffness effect on margination probability, the mean margination probabilities $< \boldsymbol{\Phi} >$ are calculated and given in figure 5(d). The mean value takes the time-averaged value of margination probability, which is estimated in a time interval within the steady-state regime. We can see that the margination process of MPs reaches steady state after about $t = 2.5\ s$. The localization of MPs at wall decreases dramatically when the particles are very stiff (small Ca). While with further decrease of stiffness (increase of Ca), there is no obvious change of the margination probability.

The underlying mechanism of this stiffness-dependency of margination behavior relies on the interplay of collision with RBCs and deformation induced lateral migration of elastic MPs (Qi & Shaqfeh 2017). At the beginning of the simulation, the RBCs near the wall of channel sense the shear flow, and then deform under the shear stress. The existence of wall makes RBCs move away from wall, and then the CFL forms. According to previous study in Katanov et al. (2015), the time needed to fully form CFL is about $0.8\ s$ under the conditions (channel size and hematocrit) in current study (Ye et al. 2017a). It signals that the first stage of margination probability corresponds to the development of CFL (c.f., figure 5(a)). In this stage, a large number of RBCs move from near wall region to center of channel. The migration of RBCs should induce reverse flow moving from center to CFL in the regions around RBCs, due to the mass conservation of the fluid. Hence, if the MPs locate in these reverse flow regions, they will move along with the flow from center to CFL. This phenomenon looks like the exclusion effect that particles are excluded by RBCs from near wall region to center of the channel (Crowl & Fogelson 2011). Specifically, the exclusion effect appears more significant for soft particles than stiff particles. Here soft MPs have stronger alignment to flow due to deformation. This is the reason why, in the first stage, the soft MPs marginate faster than stiff ones. In the second stage, the CFL is fully formed and the flow is fully developed. The soft MPs in the near wall region may experience the deformation induced migration due to the existence of the wall. This results in the low accumulation of soft MPs in the CFL. However, when the stiffness of MPs decreases to a critical value (about $Ca = 0.037$), the deformation induced migration dominates the motion of MPs. Therefore, under this circumstance, changing stiffness of MPs will not result in an obvious difference of the margination probability.

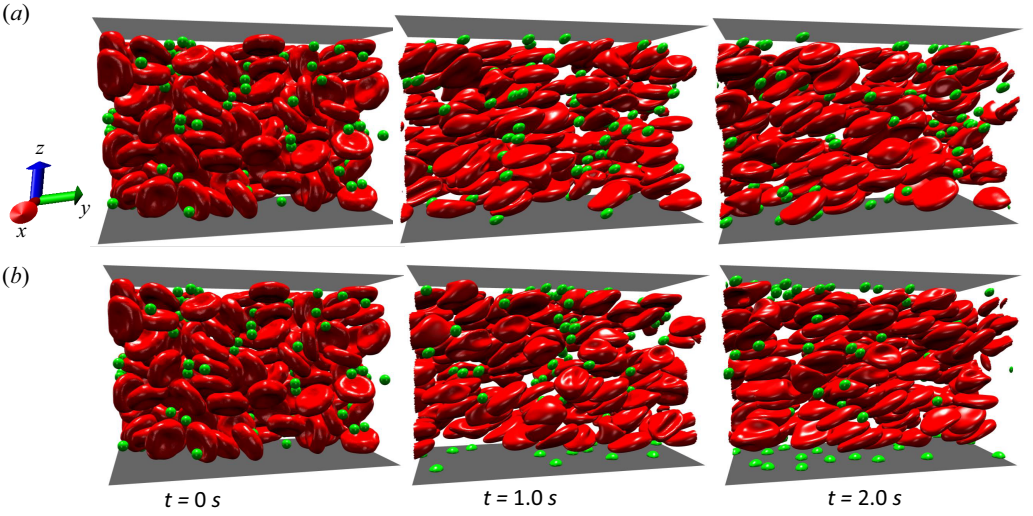

Figure 6. Snapshots for the margination behavior of elastic MPs ($Ca = 0.37$) under influence of adhesion (a) $Ad = 0.07$ and (b) $Ad = 32.8$.

4.2. Adhesion effect on localization of elastic MPs at wall

In the figure 5(a), it is obvious that the evolution of margination probability oscillates. In some time intervals, the oscillation amplitude can reach about 20% of the margination probability. It indicates that many MPs are traveling between the center of the channel and CFL. Under this circumstance, MPs near the CFL have chance to interact with the vessel wall through ligand-receptor binding. Since the diameter of MP is 2.0 μm, when it moves near the CFL, a part of its surface will locate inside the adhesion layer according to the thicknesses of CFL (2.8 μm) and adhesion layer (1.0 μm).

To have a direct comparison, figure 6 presents adhesion effect on the localization of elastic MPs. In figure 6(a), and figure 6(b), the stiffnesses of MPs are the same $Ca = 0.37$, while the adhesion strengths are different: (a) $Ad = 0.07$, and (b) $Ad = 32.8$. We find that there are more MPs entering and staying inside the CFL when increasing the adhesion strength Ad. With small $Ad = 0.07$, when MPs move into CFL, only a small contact area forms between MP and substrate. The ligand-receptor binding is not strong, and these MPs move freely near the substrate. However, with strong adhesion $Ad = 32.8$, the MPs collapse on the substrate like a droplet on the ground. It should be emphasized that this collapse phenomenon only happens for soft MPs. If the MP is stiff or rigid, it can not deform any more. They can only roll on the substrate (King & Hammer 2001; Coclite et al. 2017; Decuzzi & Ferrari 2006). While elastic MPs can either roll or firmly adhere on the substrate, depending on the adhesion strength Ad.

To differentiate the margination probability of MPs with and without adhesion, we use Π rather than Φ to represent the margination probability with adhesion effect. The interplay of stiffness and adhesion strength effects is isolated in figure 7. Figure 7(a) gives the relationship between margination probability and adhesion strength for MPs with different stiffnesses. $< \cdot >$ denotes the mean value over time interval, and subscript m represents margination. We find that the margination probabilities have the same tendencies with increment of adhesion strength for MPs with different stiffness. Under relatively low adhesion strength ($Ad < 5$), the margination probability dramatically increases with the adhesion strength increasing. While further increment of adhesion strength makes margination probability slowly decrease ($5 < Ad < 23$). But when the

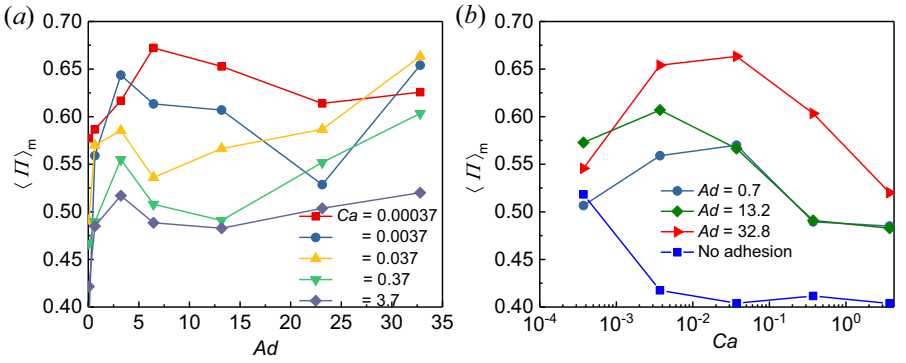

Figure 7. Margination probabilities of elastic MPs with adhesion effect. (a) Margination probability against adhesion strength with different MP stiffnesses. (b) Margination probability against MP stiffness with different adhesion strengths.

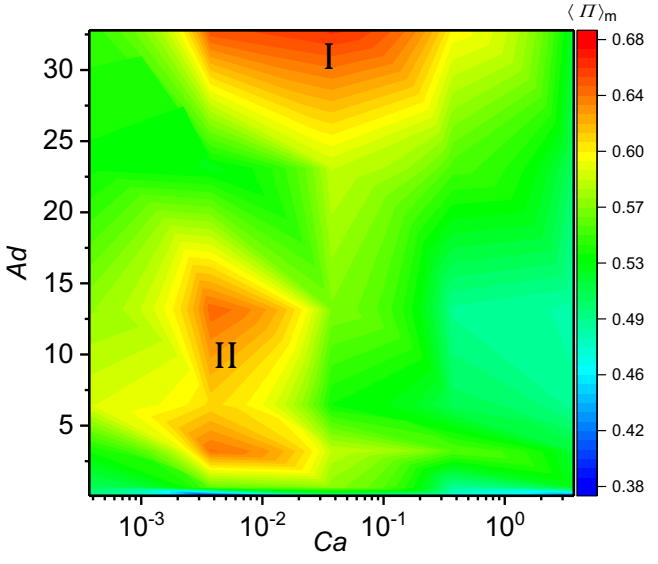

Figure 8. Contour of margination probability on the $Ca-Ad$ plane.

adhesion strength exceeds a critical value, the margination probability will increase with the increment of adhesion strength again. The critical value differs among MPs with different stiffnesses. The margination probability against stiffness is given in figure 7(b) for MPs with different adhesion strengths. The margination probability result of MP without adhesion ($Ad = 0$) is also presented to make the comparison. We find that, with the same adhesion strength, the margination probabilities increase with the increment of Ca when MPs are stiff (relatively small Ca). While further increase of Ca results in the decrease of margination probability. Though the margination probability has a decrement when the MP is soft (high Ca), it is still higher than that of MP without adhesion. And the difference of margination probability between the cases with and without adhesion is determined by the adhesion strength. These relationships remains to be discussed in detail later.

Furthermore, we summarize the results of margination probabilities in the contour on $Ca-Ad$ plane as shown in figure 8. We find that two peaks exist in the contour for

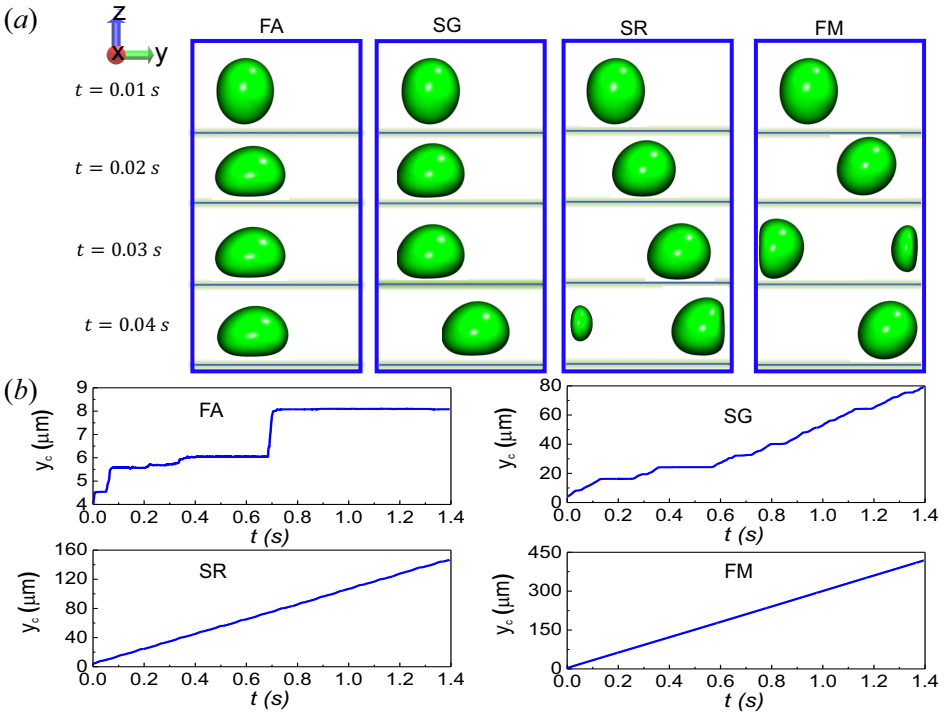

Figure 9. Identification of motion types of elastic MPs. (a) Snapshots for firm adhesion (FA), stop-go motion (SG), stable rolling (SR) and free motion (FM). (b) Corresponding trajectories of four different types of motion for elastic MPs along flow direction.

the margination probability. One is in the region with high adhesion strength Ad and moderate stiffness (moderate Ca), namely I. And the other one locates at the region with moderate adhesion strength Ad and large stiffness (small Ca), denoted as II. These two regions, which favor margination behavior, are determined by the interplay of adhesion effect and deformability. To investigate the underlying mechanisms, the adhesion behavior of elastic MPs is first examined.

4.3. Adhesion behavior of elastic MPs

The adhesion behavior should be influenced by the deformability according to previous studies (Ndri et al. 2003; Khismatullin & Truskey 2005; Balsara et al. 2016; Luo & Bai 2016; Ye et al. 2018a). The deformability of MPs can affect the hydrodynamics, which balances the spring force exerted by the biological bonds. It is revealed that deformation of MP can promote the adhesion of MP to the substrate. Previous studies (Ndri et al. 2003; Khismatullin & Truskey 2005) demonstrated that when elastic MP moved near the substrate, the bottom of MP was flattened. This resulted in a large contact area between MP and substrate. Then the adhesion became strong. Before we present the adhesion behavior of elastic MPs in blood flow, the classification of motion types of elastic MPs is shown first. On the basis of our adhesive model, probabilistic model (Hammer & Lauffenburger 1987), there are total four motion types of elastic MPs, which are presented in figure 9(a). They are characterized by the snapshots at $t = 0.01, 0.02, 0.03$ and 0.04 s along the flow (y) direction. In the firm adhesion (FA), the MP collapses on the substrate like a droplet and cannot move any more. While the MP can slowly move at some time intervals despite of collapsing on substrate in stop-and-go motion (SG).

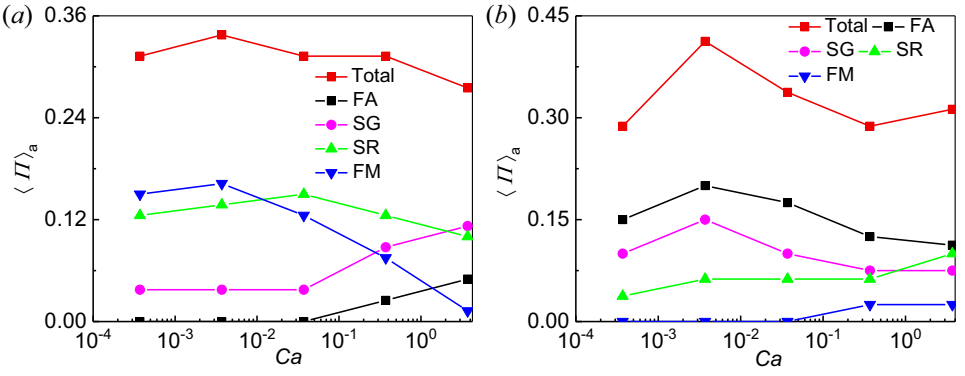

Figure 10. Adhesion probabilities for elastic MPs and corresponding adhesion probabilities of different motion types: (a) $Ad = 0.7$. (b) $Ad = 32.8$

However, in stable rolling (SR), the MP moves on the substrate. Additionally, the MP deforms like an ellipsoid under shear stress with a flattened contact area between MP and substrate. In the free motion (FM), the MP totally becomes an ellipsoid. And it moves freely near the substrate. Under FM, there is no obvious contact between MP and substrate. These motions are distinguished by calculating the velocity of the MP's center (c.f. figure 9(b)) along flow direction ($y-$direction). In FA, the velocity is nearly zero through the simulation time. When the velocity is nonzero at some time intervals and zero at the other time intervals, it is referred to SG. As for the SR and FM, there is no difference in terms of trajectories of MP's center. While their velocities are not identical. If the velocity of MP's center is the same as the fluid velocity at the same location, it is defined as FM. Otherwise, it is SR motion. The detailed classification of these adhesion types are discussed in Supporting Information.

The adhesion probability is used to quantify the behaviors of MPs near the substrate. And it is defined as:

$$\Pi_a(t) = \frac{n_a(t)}{N}, \tag{4.2}$$

where $n_a(t)$ represents the number of elastic MPs that have interactions with substrate at time t. Here, the formation of biological bond between ligand and receptor is the indication of interaction between MP and substrate. N is the total number of elastic MPs. And subscript a is adopted to distinguish it from margination probability. Additionally, the adhesion probability of the four motion types of MPs on the substrate is defined as number fraction of MPs with definite motion types. In the following, for simplicity, the type name of MPs represent the corresponding adhesion probability. Figure 10 presents the adhesion probabilities for elastic MPs and the motion types. In figure 10(a), the adhesion strength is weak ($Ad = 0.7$). We find that when the MPs are stiff (low Ca), FM and SR dominate the motion of MPs compared to SG and FA. Almost no MP has FA. But when the MPs become soft (increasing Ca), FM and SR decrease. And the FM can even vanish when Ca is large enough. While SG and FA start to increase, and SG can exceed SR and FM when MPs are very soft (high Ca). One thing should be noted that summation of adhesion probabilities of all of the four motion types should equal to the total adhesion probability. The tendency is consistent with previous studies that deformability can promote the firm adhesion of particles on the substrate (Ndri et al. 2003; Khismatullin & Truskey 2005; Shen et al. 2018). However, when the adhesion strength increases (c.f. figure 10(b)), the adhesion probabilities have the opposite trend compared to that under weak adhesion. FA and SG dominate the motion of MPs when

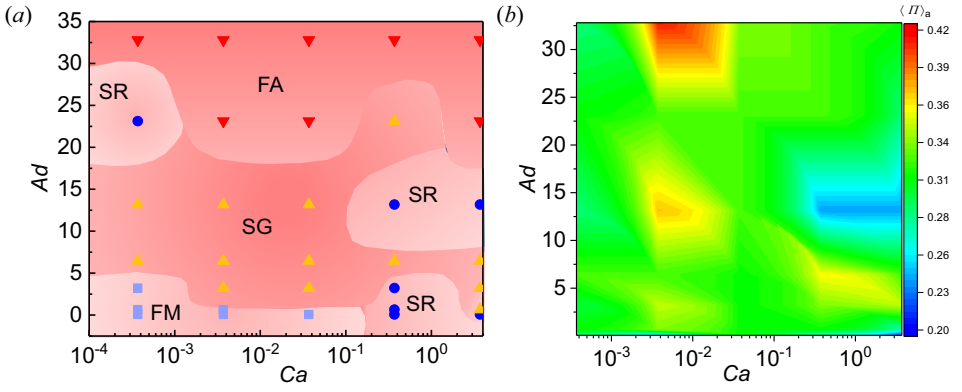

Figure 11. (a) Phase diagram for motion type of elastic MPs on $Ca-Ad$ plane. (b) Adhesion probability contour of elastic MPs on $Ca-Ad$ plane.

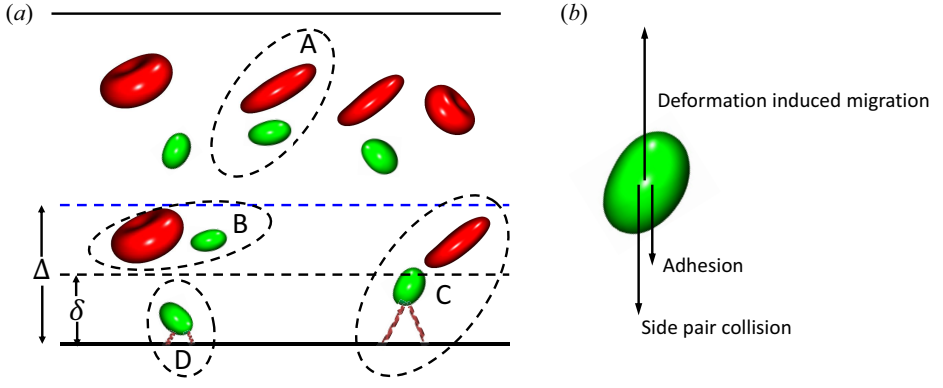

Figure 12. (a) Interaction modes of elastic MPs in blood flow. (b) Three mechanisms dominating the motion of elastic MPs near the wall of channel.

MPs are stiff. When MPs become soft (increasing Ca), SG and FA start to decrease, but SR and FM increase. When MPs are soft enough (high Ca), SR can outperform FA and SG. This results in the opposite conclusion that stiff MP demonstrates superior adhesion compared to soft particles when adhesion strength is strong.

To have detailed motion type distributions with different adhesion strengths and stiffnesses, we give the phase diagram of motion types on $Ca-Ad$ plane as shown in figure 11(a). The type is chosen as this: for example, when $Ca=0.037$ and $Ad=32.8$, adhesion probability of FA dominates compared to other three motion types, then we use FA to represent the motion type of MPs under the specific adhesion strength and stiffness. Comparing figure 11(a) with the magination probability contour under adhesion effect (c.f. figure 8), we find that the two regions favoring margination are just the FA and SG regions corresponding to motion type phase diagram. It means that adhesion favoring region is also the margination favoring region. Additionally, the adhesion probability contour is provided in figure 11(b). We find that in the regions where the margination probabilities are high, the adhesion probabilities are also high. The high margination should be prerequisite for the high adhesion, but the intrinsic relationship between margination and adhesion is not clear. We will discuss it in detail below.

4.4. Mechanism of localization of elastic MPs under adhesion

When the elastic MP locates in the blood flow, it can interact with other objects, such as RBCs, wall of the channel and other MPs. Particularly, considering adhesion effect, the elastic MP can also interact with wall through ligand-receptor binding. We give a simple schematic to show the interaction modes of elastic MP with other objects in figure 12(a). Here, the interaction mode between MP and MP is negligible due to the low volume fraction (less than 1%). When the MP locates in the center region of channel, it can only interact with RBCs through hydrodynamic collision, which is denoted as interaction mode A in the figure. We define a near wall region Δ, in which the existence of wall will influence the motion of objects within it. The thickness of Δ is about 3 times of the radius of the object (Singh et al. 2014). If the MP enters the region Δ, it can experience the deformation induced migration besides the hydrodynamic collision with RBC. We name this mode as B. Further moving towards the wall makes elastic MP locate around the interface of CFL (δ). MP in this region has complicated interactions with its surroundings. It not only collides with RBC and experiences the deformation induced migration, but also starts to interact with wall through ligand-receptor binding. The interaction mode in this region is symbolized as C. While after the MP moves into the CFL and adheres on the substrate, it experiences both adhesive interaction and deformation induced migration. We call this interaction mode D. We focus on the mode C and isolate it in figure 12(b). Here we believe that the motion of elastic MP with mode C is complex but crucial to margination and adhesion process. The region, where this mode happens, locates around the interface of the CFL and adhesion layer. If MP moves away from the wall, it will not be counted as MP having localization. While when it moves towards the wall, it will be regarded as MP owning margination and adhesion. The moving direction is attributed to the competition of three mechanisms: (i) deformation induced migration; (ii) adhesion effect; and (iii) near-wall hydrodynamic collision with RBC. The deformation induced migration makes MP move away from wall, and thus hampers the localization. The adhesion effect plays a role through biological bond, and it facilitates localization. As for the near-wall hydrodynamic collision with RBC, because there is no RBC within CFL, then the collision should be one side collision. The RBCs always locate in one side of the MP. Furthermore, it is confirmed that three-body and higher order collision schemes can be negligible under current circumstance ($Ht = 30\%$) (Kumar & Graham 2012a; Rivera et al. 2016; Qi & Shaqfeh 2017). Therefore, only side pair collision is considered here. According to the locations of RBC and MP, the pair collision hinders the penetration of MP into center of channel, and thus promotes the localization.

The side pair collision is first examined systematically for elastic MPs with different stiffnesses. Figure 13(a) gives the side pair collision illustration. In this numerical experiment, the channel and the flow condition are the same as above simulations for margination of elastic MPs. A single RBC and an elastic MP are placed in the center of the channel to eliminate the wall effect. The center distance between their initial positions in height direction (z-direction) is $\sigma = 2\ \mu m$. During the simulation, the trajectories of centers of RBC and MP are tracked. And the displacement of centers of RBC and MP in z-direction refers to the collision displacement. The evolution of collision displacements for RBC (Δ_R) and elastic MP (Δ_S) are presented in figure 13(b). As for the RBC, we find that the collision displacements are almost the same. And they are much smaller compared to all of the elastic MPs. They have no dependence on the stiffness of MPs. This is attributed to the small size of MP compared to the RBC. The trajectories of MPs with different stiffnesses have the same trend. The first approaching between

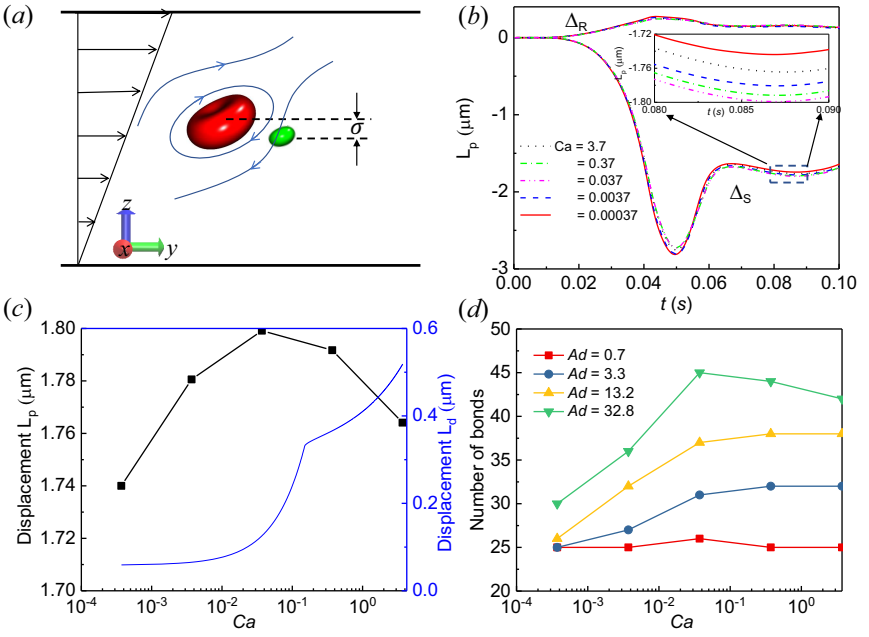

Figure 13. (a) Numerical experiment for pair collision between RBC and elastic MP. (b) Collision displacement of RBC and elastic MP with different stiffnesses. (c) Comparison of collision displacement and deformation induced migration displacement of elastic MPs. (d) Number of biological bonds established when elastic MPs on substrate against stiffness of elastic MP with different adhesion strengths.

RBC and MP makes the MP abruptly migrate towards the wall. After collision ends, it can partially restore towards its initial position. It locates in a specific equilibrium position between the initial and maximum migration positions. We denote the distance between this equilibrium position and initial position as the collision displacement, which is based on the definition in Refs. (Kumar & Graham 2012b,a, 2011; Zhao & Shaqfeh 2013; Loewenberg & Hinch 1997). From the zoom-out in figure 13(b), we can see the difference of collision displacements among MPs with different stiffnesses is small. But this is individual collision between RBC and MP. The repeated collision between RBC and MP will distinguish the collision displacement with large value for MPs with different stiffnesses. The result is shown in figure 13(c). L_p represents the collision displacement. We find that when $Ca < 0.037$, the collision displacement increases with the increment of Ca, while when $Ca > 0.037$, it decreases slightly with the increment of Ca. Hence, there is an optimal stiffness for the pair collision of elastic MP and RBC (Results in Supporting Information points that this optimal Ca is a bit larger than 0.037).

As far as we know, this is the first time to present the hydrodynamic collision between RBC and elastic MP. There are also a number of previous studies showing the pair collision between particles with either same volume or same shape (Kumar & Graham 2011, 2012b; Sinha & Graham 2016). The collision result can be explained as follows. Due to the size difference between RBC (diameter 8 μm) and elastic MP (diameter 2 μm), the motion of elastic MP is likely governed by the fluctuation of flow field near RBC induced by its deformation. RBC should make tank treading motion under shear flow, and the flow field around it is presented in figure 13(a). When $Ca < 0.037$, with the increment of Ca, soft MP is easier to align itself to flow field, thus the collision displacement increases. However, further increase of Ca makes the tank treading motion of soft MP become

significant (Fedosov et al. 2010a). The tank treading motion of soft MP can also induce the fluctuation of flow around it, but with the opposite direction to flow field induced by RBC motion. It acts as resistance to the alignment of MP to flow field. Therefore, further increase of Ca will lead to the decrease of the collision displacement of MP.

When elastic MP is placed in the flow, the shape cannot be analytically captured, especially for the MP with large deformation. Therefore, the deformation induced migration, which is highly dependent on the shape of MP, can be hardly determined. In literature, numerical simulations are employed to study the deformation induced migration of elastic MP in the flow (Singh et al. 2014; Doddi & Bagchi 2008; Kaoui et al. 2008; Nix et al. 2014; Qi & Shaqfeh 2017). Here, an empirical relationship in Singh et al. (2014) is adopted, due to its systematics. In their study, the lateral migration velocity of the deformable capsule is a function of its stiffness (Ca) and distance away from the wall (h). A phenomenological formula for migration velocity is given as:

$$\frac{V_d}{\dot{\gamma}a} = \begin{cases} (0.65Ca + 0.021)(\frac{a}{h})^2, & Ca \leqslant Ca_{\rm cr} \\ V^*_{cr} + 0.02(Ca - Ca_{\rm cr})^{0.6}(\frac{a}{h})^{1.35}, & Ca > Ca_{\rm cr}, \end{cases} \tag{4.3}$$

where $V^*_{cr} = \frac{V_d}{\dot{\gamma}a}|_{Ca=Ca_{\rm cr}}$. Their simulation results pointed out a power law relation for the capsule velocity. There exists a critical stiffness, $Ca_{\rm cr}$ of the capsule, here we choose it as $Ca_{\rm cr} = 0.15$ according to the proposed regime in Singh et al. (2014). When $Ca \leqslant Ca_{\rm cr}$, the migration velocity is linearly proportional to Ca and related to h^{-2}, while when $Ca > Ca_{\rm cr}$, the velocity has 0.6 and -1.35 power scalings with Ca and h, respectively. On the basis of this relation, we set $h = 2\ \mu m$, which corresponds to the position between adhesion layer and CFL, and then integrate Eq. (4.3) from $t = 0$ to $t = 0.1$. The deformation induced migration displacement L_d against stiffness of elastic MP is obtained and shown in figure 13(c), denoted as a blue line.

To study the adhesion effect, we also conduct simulation experiments to investigate the adhesion behavior of a single elastic MP on substrate under shear flow. The flow and the channel size are the same with the above margination study. Because the interaction between an elastic MP and substrate is established by the biological bonds formed in the adhesion process, and the bond is modeled as linear spring. The number of bonds can be used to quantify the adhesion effect. Figure 13(d) shows the relationship between number of bonds and stiffness of elastic MP under different adhesion strengths. We find that the number of bonds increases with the increment of Ca when the Ca is not large ($Ca < 0.037$). However, further increase of Ca does not significantly affect the number of bonds. When adhesion strength is very strong ($Ad = 32.8$), the number of bonds may slightly decrease with increment of Ca.

The results given above demonstrate the strength of three mechanisms against the stiffness of MPs. They are combined to explain the margination results in figure 7(b). When the MP is relatively stiff (low $Ca < 0.037$), with the increment of Ca, the collision displacement increases, adhesion effect increases, and the deformation induced migration displacement almost keeps unchanged. Two promotion factors of localization increase and one impediment factor keeps unchanged. Thus, the margination probability increases with the increment of Ca. However, when Ca exceeds the critical value $Ca = 0.037$, the MP becomes relatively soft. With the increment of Ca, the collision displacement decreases, adhesion effect almost keeps unchanged, and the deformation induced migration drastically increases. The impediment factor of localization dominates compared to the other two promotion factors. Hence, under this circumstance, the localization of MP decreases with the increment of Ca.

Furthermore, the relationship between margination behavior and adhesion strength

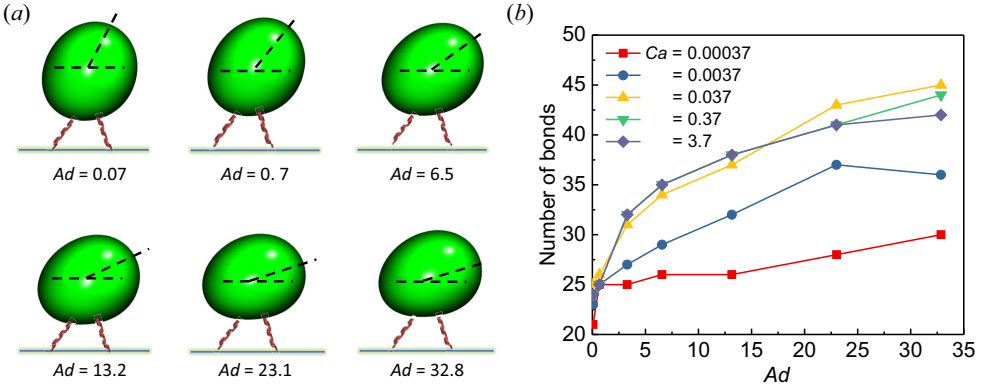

Figure 14. (a) Deformation of particles with $Ca = 0.037$ under different adhesion strengths. Dashed lines are used to guide the deformation of particles. (b) Number of biological bonds established when elastic MPs adhere on substrate against adhesion strengths for particles with different stiffnesses.

is isolated to investigate. With the same Ca, the side pair collision displacements for MPs under different adhesion strengths should be the same, because the collision displacements is independent on the adhesion. While the deformation induced migration displacement should be influenced by the adhesion strength. From Eq. (4.3), it seems that the deformation induced migration velocity is only relevant to Ca. But this is not true. The root cause of deformation induced migration is the deformation of MP under shear flow. Here, considering adhesion effect, the deformation of MP is affected by not only Ca, but also the adhesion strength Ad. Figure 14(a) presents the configurations of MP with the same $Ca = 0.037$, but under different adhesion strengths. We find that, when the adhesion strength is weak ($Ad = 0.07$), the deformation of MP is small. With the increment of adhesion strength ($Ad = 0.7 - 13.2$), the deformation becomes significant and increases. While further increase of Ad will not cause any further increment of MP deformation. This result reveals that adhesion effect plays a role in the localization of MPs through influencing the deformation of MP. Additionally, relationship between number of bonds and adhesion strength for MPs with different stiffnesses is displayed in the figure 14(b). We find that, when the adhesion strength is small ($Ad < 3.3$), the number of bonds dramatically increases with the increment of Ad. While, further increment of Ad also results in the increase of number of bonds, but with a slow growth rate.

Apart from the collision effect, adhesion effect and deformation induced migration are combined to reveal the underlying mechanism of margination probability against adhesion strength for MPs with different stiffnesses in figure 7(a). When Ad is small ($Ad \sim 0.7$), the deformation induced migration displacements are almost the same, but the adhesion effect dramatically increases, thus the margination probability grows fast with the increment of adhesion strength. When Ad becomes relatively large ($Ad \sim 0.7 - 13.2$), the adhesion effect slowly increases, while the deformation of particles is significant, leading to large deformation induced migration displacement. Therefore, in this regime, the margination probability decreases with the increment of adhesion strength. With the further increase of Ad, the deformation induced migration displacements are almost constant, but adhesion effects still slowly increase. Hence, the margination probability should increase with the increment of adhesion strength in this regime.

5. Conclusion

We present the numerical results on the localization of elastic MPs without and with effect of adhesion. Margination probability is adopted to quantify the localization of elastic MPs. Without adhesion effects, margination probabilities of MPs decrease with the increment of Ca. This stiffness-dependency of margination behavior is found to rely on the interplay of collision with RBCs and deformation induced lateral migration of elastic MPs. We find that the evolution of margination can be split into two stages. The first stage corresponds to the development of CFL. And in this stage, soft MP marginates more readily than the stiff one. It is attributed to the exclusion of RBCs moving from CFL to the center of the channel. The volume exclusion effect is more significant for soft MPs than that of the stiff MPs, because deformation of soft MPs demonstrate stronger alignment to the flow direction. However, in the second stage, the CFL is fully formed and the flow is fully developed. The soft MPs in the near wall region will experience the deformation induced migration due to the existence of the wall. This results in the low accumulation of soft MPs in CFL. Thus, the margination probability decreases with the increment of Ca. After the MP becomes softer (high Ca), the deformation induced lateral migration dominates the motion of MPs, therefore, the margination probabilities almost keep the same with the change of Ca.

Furthermore, localization of elastic MPs under adhesion effect is studied. We obtain the margination probability contour by systematically varying capillary number Ca and adhesion number Ad. We find that there are two optimal regimes favoring high margination probability on the $Ca-Ad$ plane. It is concluded that the existence of optimal regimes is induced by the interplay of MP deformability and adhesion. The underlying mechanism is explained as competition among three factors: (i) near-wall hydrodynamic collisions between RBCs and MPs; (ii) deformation induced migration due to existence of wall; (iii) adhesive interaction between MPs and substrate. For MPs with same adhesion strengths Ad, when they are relatively stiff (low $Ca = 0.00037 \sim 0.037$), the collision displacements increase with the increment of Ca. At the same time, the adhesion effects increase. The deformation induced migration displacements almost keep the same. Thus, the margination probability will increase with the increment of Ca. However, after Ca of MPs exceeds the critical value $Ca = 0.037$, the MPs become softer. With the increment of Ca, the collision displacements decrease and the adhesion effects have no obvious difference, while deformation induced migration displacements dramatically increase. Hence, the margination probability decreases with the increment of Ca. Additionally, the dependence of adhesion effect is investigated by fixing the stiffness of MP. As the collision displacement only depends on the stiffness of MP, we ignore its influence here. When Ad is small, the deformation induced migration displacements are almost the same, while the adhesion effects increase quickly, then the margination probabilities dramatically increase with the increment of Ad. Furthermore, when Ad becomes relatively large, the adhesion effects slowly increase, while the deformation of MPs is significant. Therefore, in this regime, the margination probabilities decrease with the increase of Ad. With the further increase of Ad, the deformation induced migration displacements are almost the same. Although the growth rates are small, adhesion effects continuously increase. Thus, the margination probabilities can slowly increase with the increment of Ad.

As computational studies of the blood flow, there still exist some limitations in current numerical model. In normal human vasculature, the viscosity inside the RBC is 4 to 6 times larger than the plasma outside the RBC. This viscosity contrast can affect the rheology of the RBC suspension. This is one of the reasons why our simulation results are not exactly the same with experimental results in the validation part. Besides, the

blood vessel is usually tubular. Thus, the results obtained from the rectangular channel in our model may have some discrepancies with those in the tube. It is deserved to investigate the tube flow in the future.

The findings in this work, especially the optimal regimes favoring localization, suggest that softer MP or stronger adhesion is not always the best choice for the localization of MPs. It could offer further guidance to design efficient drug carriers in biomedical application, in which high localization is needed.

Acknowledgments

This work was supported by National Science Foundation (OAC-1755779). The authors thank Alessandro Fisher for proofreading of this work. Z. S., H. Y. and Y. L. are grateful for the support from Department of Mechanical Engineering at the University of Connecticut. Z. S. and H. Y. acknowledge the partial financial supports from the GE Fellowship for Innovation. This research benefited in part from the computational resources and staff contributions provided by the Booth Engineering Center for Advanced Technology (BECAT) at the University of Connecticut. Part of this work used the Extreme Science and Engineering Discovery Environment (XSEDE), which is supported by the National Science Foundation grant number ACI-1053575.

REFERENCES

Abkarian, Manouk, Lartigue, Colette & Viallat, Annie 2002 Tank treading and unbinding of deformable vesicles in shear flow: determination of the lift force. Phys. Rev. Lett. 88 (6), 068103.

Aidun, Cyrus K & Clausen, Jonathan R 2010 Lattice-boltzmann method for complex flows. Annual review of fluid mechanics 42, 439–472.

Allen, Mike P & Tildesley, Dominic J 1989 Computer simulation of liquids. Oxford university press.

Balsara, Hiren D, Banton, Rohan J & Eggleton, Charles D 2016 Investigating the effects of membrane deformability on artificial capsule adhesion to the functionalized surface. Biomech. Model. Mechanobiol. 15 (5), 1055–1068.

Bell, George I 1978 Models for the specific adhesion of cells to cells. Science 200 (4342), 618–627.

Benzi, Roberto, Succi, Sauro & Vergassola, Massimo 1992 The lattice boltzmann equation: theory and applications. Phys. Rep. 222 (3), 145–197.

Bernaschi, Massimo, Melchionna, Simone, Succi, Sauro, Fyta, Maria, Kaxiras, Efthimios & Sircar, Joy K 2009 Muphy: A parallel multi physics/scale code for high performance bio-fluidic simulations. Comput. Phys. Commun. 180 (9), 1495–1502.

Bhagat, Ali Asgar S, Bow, Hansen, Hou, Han Wei, Tan, Swee Jin, Han, Jongyoon & Lim, Chwee Teck 2010 Microfluidics for cell separation. Med. Biol. Eng. Comput. 48 (10), 999–1014.

Borgdorff, Joris, Mamonski, Mariusz, Bosak, Bartosz, Kurowski, Krzysztof, Belgacem, M Ben, Chopard, Bastien, Groen, Derek, Coveney, Peter V & Hoekstra, Alfons G 2014 Distributed multiscale computing with muscle 2, the multiscale coupling library and environment. J. Comput. Sci 5 (5), 719–731.

Bretherton, Francis P 1962 The motion of rigid particles in a shear flow at low reynolds number. J. Fluid Mech. 14 (2), 284–304.

Callens, Natacha, Minetti, Christophe, Coupier, G, Mader, M-A, Dubois, Frank, Misbah, Chaouqi & Podgorski, Thomas 2008 Hydrodynamic lift of vesicles under shear flow in microgravity. Europhys. Lett. 83 (2), 24002.

Cantat, Isabelle & Misbah, Chaouqi 1999 Lift force and dynamical unbinding of adhering vesicles under shear flow. Phys. Rev. Lett. 83 (4), 880.

Charoenphol, Phapanin, Huang, Ryan B & Eniola-Adefeso, Omolola 2010 Potential role of

size and hemodynamics in the efficacy of vascular-targeted spherical drug carriers. Biomaterials 31 (6), 1392–1402.

Charoenphol, Phapanin, Onyskiw, Peter J, Carrasco-Teja, Mariana & Eniola-Adefeso, Omolola 2012 Particle-cell dynamics in human blood flow: implications for vascular-targeted drug delivery. J. Biomech. 45 (16), 2822–2828.

Chen, Shiyi & Doolen, Gary D 1998 Lattice boltzmann method for fluid flows. Annu. Rev. Fluid Mech. 30 (1), 329–364.

Clausen, Jonathan R, Reasor Jr, Daniel A & Aidun, Cyrus K 2010 Parallel performance of a lattice-boltzmann/finite element cellular blood flow solver on the ibm blue gene/p architecture. Comput. Phys. Commun. 181 (6), 1013–1020.

Coclite, A, Mollica, H, Ranaldo, S, Pascazio, G, de Tullio, MD & Decuzzi, P 2017 Predicting different adhesive regimens of circulating particles at blood capillary walls. Microfluid. Nanofluid. 21 (11), 168.

Coupier, Gwennou, Kaoui, Badr, Podgorski, Thomas & Misbah, Chaouqi 2008 Noninertial lateral migration of vesicles in bounded poiseuille flow. Phys. Fluids 20 (11), 111702.

Crowl, L & Fogelson, Aaron L 2011 Analysis of mechanisms for platelet near-wall excess under arterial blood flow conditions. J. Fluid Mech. 676, 348–375.

Czaja, B, Závodszky, G, Tarksalooyeh, V Azizi & Hoekstra, AG 2018 Cell-resolved blood flow simulations of saccular aneurysms: effects of pulsatility and aspect ratio. Journal of The Royal Society Interface 15 (146), 20180485.

Danker, Gerrit, Vlahovska, Petia M & Misbah, Chaouqi 2009 Vesicles in poiseuille flow. Phys. Rev. Lett. 102 (14), 148102.

Dao, M, Li, J & Suresh, S 2006 Molecularly based analysis of deformation of spectrin network and human erythrocyte. Mater. Sci. Eng. C 26 (8), 1232–1244.

Decuzzi, P & Ferrari, Mauro 2006 The adhesive strength of non-spherical particles mediated by specific interactions. Biomaterials 27 (30), 5307–5314.

Decuzzi, P, Godin, Biana, Tanaka, T, Lee, S-Y, Chiappini, C, Liu, X & Ferrari, Mauro 2010 Size and shape effects in the biodistribution of intravascularly injected particles. J. Controlled Release 141 (3), 320–327.

Doddi, Sai K & Bagchi, Prosenjit 2008 Lateral migration of a capsule in a plane poiseuille flow in a channel. Int. J. Multiphase Flow 34 (10), 966–986.

marquis Du Trochet, Henri 1824 Recherches anatomiques et physiologiques sur la structure intime des animaux et des végétaux, et sur leur motilité. JB Baillière.

Evans, Evan A & Skalak, Richard 1980 Mechanics and thermodynamics of biomembranes. CRC Press, Inc., Boca Raton, Florida.

Fåhraeus, Robin 1929 The suspension stability of the blood. Physiol. Rev. 9 (2), 241–274.

Fåhræus, Robin & Lindqvist, Torsten 1931 The viscosity of the blood in narrow capillary tubes. Am. J. Physiol. 96 (3), 562–568.

Farutin, Alexander & Misbah, Chaouqi 2011 Symmetry breaking of vesicle shapes in poiseuille flow. Phys. Rev. E 84 (1), 011902.

Farutin, Alexander & Misbah, Chaouqi 2013 Analytical and numerical study of three main migration laws for vesicles under flow. Phys. Rev. Lett. 110 (10), 108104.

Fay, Meredith E, Myers, David R, Kumar, Amit, Turbyfield, Cory T, Byler, Rebecca, Crawford, Kaci, Mannino, Robert G, Laohapant, Alvin, Tyburski, Erika A, Sakurai, Yumiko & others 2016 Cellular softening mediates leukocyte demargination and trafficking, thereby increasing clinical blood counts. Proc. Natl. Acad. Sci. U.S.A. 113 (8), 1987–1992.

Fedosov, Dmitry A 2010 Multiscale modeling of blood flow and soft matter. Brown University.

Fedosov, Dmitry A, Caswell, Bruce & Karniadakis, George Em 2010a A multiscale red blood cell model with accurate mechanics, rheology, and dynamics. Biophys. J. 98 (10), 2215–2225.

Fedosov, Dmitry A, Caswell, Bruce & Karniadakis, George Em 2011a Wall shear stress-based model for adhesive dynamics of red blood cells in malaria. Biophys. J. 100 (9), 2084–2093.

Fedosov, Dmitry A, Caswell, Bruce, Popel, Aleksander S & Karniadakis, George Em 2010b Blood flow and cell-free layer in microvessels. Microcirculation 17 (8), 615–628.

Fedosov, Dmitry A, Fornleitner, Julia & Gompper, Gerhard 2012 Margination of white blood cells in microcapillary flow. Phys. Rev. Lett. 108 (2), 028104.

Fedosov, Dmitry A, Pan, Wenxiao, Caswell, Bruce, Gompper, Gerhard & Karniadakis, George E

2011b Predicting human blood viscosity in silico. Proc. Natl. Acad. Sci. U.S.A. 108 (29), 11772–11777.

Fogelson, Aaron L & Neeves, Keith B 2015 Fluid mechanics of blood clot formation. Annu. Rev. Fluid Mech. 47, 377–403.

Freund, Jonathan B 2007 Leukocyte margination in a model microvessel. Phys. Fluids 19 (2), 023301.

Gossett, Daniel R, Weaver, Westbrook M, Mach, Albert J, Hur, Soojung Claire, Tse, Henry Tat Kwong, Lee, Wonhee, Amini, Hamed & Di Carlo, Dino 2010 Label-free cell separation and sorting in microfluidic systems. Anal. Bioanal.Chem. 397 (8), 3249–3267.

Guo, Zhaoli, Zheng, Chuguang & Shi, Baochang 2002 Discrete lattice effects on the forcing term in the lattice boltzmann method. Phys. Rev. E 65 (4), 046308.

de Haan, Mike, Zavodszky, Gabor, Azizi, Victor & Hoekstra, Alfons 2018 Numerical investigation of the effects of red blood cell cytoplasmic viscosity contrasts on single cell and bulk transport behaviour. Appl. Sci. 8 (9), 1616.

Hammer, Daniel A 2014 Adhesive dynamics. J. Biomech. Eng. 136 (2), 021006.

Hammer, DANIEL A & Lauffenburger, DOUGLAS A 1987 A dynamical model for receptor-mediated cell adhesion to surfaces. Biophys. J. 52 (3), 475–487.

Higuera, FJ, Succi, S & Benzi, R 1989 Lattice gas dynamics with enhanced collisions. EPL (Europhysics Letters) 9 (4), 345.

Hou, Han Wei, Bhagat, Ali Asgar S, Chong, Alvin Guo Lin, Mao, Pan, Tan, Kevin Shyong Wei, Han, Jongyoon & Lim, Chwee Teck 2010 Deformability based cell margination–simple microfluidic design for malaria-infected erythrocyte separation. Lab. Chip 10 (19), 2605–2613.

Kantsler, Vasiliy, Segre, Enrico & Steinberg, Victor 2008 Dynamics of interacting vesicles and rheology of vesicle suspension in shear flow. Europhys. Lett. 82 (5), 58005.

Kaoui, Badr, Ristow, GH, Cantat, Isabelle, Misbah, Chaouqi & Zimmermann, Walter 2008 Lateral migration of a two-dimensional vesicle in unbounded poiseuille flow. Phys. Rev. E 77 (2), 021903.

Katanov, Dinar, Gompper, Gerhard & Fedosov, Dmitry A 2015 Microvascular blood flow resistance: role of red blood cell migration and dispersion. Microvasc. Res. 99, 57–66.

Khismatullin, Damir B & Truskey, George A 2005 Three-dimensional numerical simulation of receptor-mediated leukocyte adhesion to surfaces: Effects of cell deformability and viscoelasticity. Phys. Fluids 17 (3), 031505.

King, Michael R & Hammer, Daniel A 2001 Multiparticle adhesive dynamics: hydrodynamic recruitment of rolling leukocytes. Proc. Natl. Acad. Sci. U.S.A. 98 (26), 14919–14924.

Koumoutsakos, Petros, Pivkin, Igor & Milde, Florian 2013 The fluid mechanics of cancer and its therapy. Annu. Rev. Fluid Mech. 45.

Krüger, Timm, Kaoui, Badr & Harting, Jens 2014 Interplay of inertia and deformability on rheological properties of a suspension of capsules. J. Fluid Mech. 751, 725–745.

Krüger, Timm, Varnik, Fathollah & Raabe, Dierk 2011 Efficient and accurate simulations of deformable particles immersed in a fluid using a combined immersed boundary lattice boltzmann finite element method. Comput. Math. Appl. 61 (12), 3485–3505.

Kumar, Amit & Graham, Michael D 2011 Segregation by membrane rigidity in flowing binary suspensions of elastic capsules. Phys. Rev. E 84 (6), 066316.

Kumar, Amit & Graham, Michael D 2012a Margination and segregation in confined flows of blood and other multicomponent suspensions. Soft Matter 8 (41), 10536–10548.

Kumar, Amit & Graham, Michael D 2012b Mechanism of margination in confined flows of blood and other multicomponent suspensions. Phys. Rev. Lett. 109 (10), 108102.

Lee, Tae-Rin, Choi, Myunghwan, Kopacz, Adrian M, Yun, Seok-Hyun, Liu, Wing Kam & Decuzzi, Paolo 2013 On the near-wall accumulation of injectable particles in the microcirculation: smaller is not better. Sci. Rep. 3, 2079.

Ley, Klaus & Tedder, Thomas F 1995 Leukocyte interactions with vascular endothelium. new insights into selectin-mediated attachment and rolling. J. Immunol. 155 (2), 525–528.

Li, Ying, Lian, Yanping, Zhang, Lucy T, Aldousari, Saad M, Hedia, Hassan S, Asiri, Saeed A & Liu, Wing Kam 2016 Cell and nanoparticle transport in tumour microvasculature: the role of size, shape and surface functionality of nanoparticles. Interface focus 6 (1), 20150086.

Liu, Yaling & Liu, Wing Kam 2006 Rheology of red blood cell aggregation by computer simulation. J. Comput. Phys. 220 (1), 139–154.

Loewenberg, M & Hinch, EJ 1997 Collision of two deformable drops in shear flow. J. Fluid Mech. 338, 299–315.

Lorenz, Eric, Hoekstra, Alfons G & Caiazzo, Alfonso 2009 Lees-edwards boundary conditions for lattice boltzmann suspension simulations. Phys. Rev. E 79 (3), 036706.

Luo, Zheng Yuan & Bai, Bo Feng 2016 State diagram for adhesion dynamics of deformable capsules under shear flow. Soft Matter 12 (33), 6918–6925.

Mackay, FE, Ollila, Santtu TT & Denniston, Colin 2013 Hydrodynamic forces implemented into lammps through a lattice-boltzmann fluid. Comput. Phys. Commun. 184 (8), 2021–2031.

Macmeccan, RM, Clausen, JR, Neitzel, GP & Aidun, CK 2009 Simulating deformable particle suspensions using a coupled lattice-boltzmann and finite-element method. J. Fluid Mech. 618, 13.

Marth, Wieland, Aland, Sebastian & Voigt, Axel 2016 Margination of white blood cells: a computational approach by a hydrodynamic phase field model. J. Fluid Mech. 790, 389–406.

Melchionna, Simone, Bernaschi, Massimo, Succi, Sauro, Kaxiras, Efthimios, Rybicki, Frank J, Mitsouras, Dimitris, Coskun, Ahmet U & Feldman, Charles L 2010 Hydrokinetic approach to large-scale cardiovascular blood flow. Comput. Phys. Commun. 181 (3), 462–472.

Mittal, Rajat & Iaccarino, Gianluca 2005 Immersed boundary methods. Annu. Rev. Fluid Mech. 37, 239–261.

Müller, Kathrin, Fedosov, Dmitry A & Gompper, Gerhard 2014 Margination of micro-and nano-particles in blood flow and its effect on drug delivery. Sci. Rep. 4, 4871.

Müller, Kathrin, Fedosov, Dmitry A & Gompper, Gerhard 2016 Understanding particle margination in blood flow–a step toward optimized drug delivery systems. Med. Eng. Phys. 38 (1), 2–10.

Ndri, NA, Shyy, W & Tran-Son-Tay, R 2003 Computational modeling of cell adhesion and movement using a continuum-kinetics approach. Biophys. J. 85 (4), 2273–2286.

Neri, Dario & Bicknell, Roy 2005 Tumour vascular targeting. Nat. Rev. Cancer 5 (6), 436.

Nix, S, Imai, Y, Matsunaga, D, Yamaguchi, T & Ishikawa, T 2014 Lateral migration of a spherical capsule near a plane wall in stokes flow. Phys. Rev. E 90 (4), 043009.

Olla, Piero 1997a The lift on a tank-treading ellipsoidal cell in a shear flow. J. Phys. II 7 (10), 1533–1540.

Olla, Piero 1997b The role of tank-treading motions in the transverse migration of a spheroidal vesicle in a shear flow. J. Phys. A: Math. Gen. 30 (1), 317.

Ollila, Santtu TT, Denniston, Colin, Karttunen, Mikko & Ala-Nissila, Tapio 2011 Fluctuating lattice-boltzmann model for complex fluids. J. Chem. Phys. 134 (6), 064902.

Persson, Per-Olof 2005 Mesh generation for implicit geometries. PhD thesis, Massachusetts Institute of Technology.

Persson, Per-Olof & Strang, Gilbert 2004 A simple mesh generator in matlab. SIAM review 46 (2), 329–345.

Peskin, Charles S 2002 The immersed boundary method. Acta Numer. 11, 479–517.

Plimpton, Steve 1995 Fast parallel algorithms for short-range molecular dynamics. J. Comput. Phys. 117 (1), 1–19.

Poiseuille, Jean Louis Marie 1836 Recherches sur les causes du mouvement du sang dans les vaisseaux capillaires. Ann. Sci. Nat. 5, 111–115.

Pries, AR, Neuhaus, D & Gaehtgens, P 1992 Blood viscosity in tube flow: dependence on diameter and hematocrit. American Journal of Physiology Heart and Circulatory Physiology 263 (6), H1770–H1778.

Pries, AR, Secomb, TW, Gessner, T, Sperandio, MB, Gross, JF & Gaehtgens, P 1994 Resistance to blood flow in microvessels in vivo. Circ. Res. 75 (5), 904–915.

Qi, Qin M & Shaqfeh, Eric SG 2017 Theory to predict particle migration and margination in the pressure-driven channel flow of blood. Phys. Rev. Fluids 2 (9), 093102.

Ramakrishnan, N, Wang, Yaohong, Eckmann, David M, Ayyaswamy, Portonovo S & Radhakrishnan, R 2017 Motion of a nano-spheroid in a cylindrical vessel flow: Brownian and hydrodynamic interactions. J. Fluid Mech. 821, 117–152.

Rivera, Rafael G Henríquez, Zhang, Xiao & Graham, Michael D 2016 Mechanistic theory of

margination and flow-induced segregation in confined multicomponent suspensions: simple shear and poiseuille flows. Phys. Rev. Fluids 1 (6), 060501.

Schnitzer, Jan E 1998 Vascular targeting as a strategy for cancer therapy. N. Engl. J. Med. 339 (7), 472–474.

Secomb, Timothy W, Styp-Rekowska, Beata & Pries, Axel R 2007 Two-dimensional simulation of red blood cell deformation and lateral migration in microvessels. Ann. Biomed. Eng. 35 (5), 755–765.

Seifert, Udo 1999 Hydrodynamic lift on bound vesicles. Phys. Rev. Lett. 83 (4), 876.

Shen, Zhiqiang, Ye, Huilin, Kröger, Martin & Li, Ying 2018 Aggregation of polyethylene glycol polymers suppresses receptor-mediated endocytosis of pegylated liposomes. Nanoscale 10 (9), 4545–4560.

Singh, Rajesh Kumar, Li, Xiaoyi & Sarkar, Kausik 2014 Lateral migration of a capsule in plane shear near a wall. J. Fluid Mech. 739, 421–443.

Singh, Rajesh Kumar & Sarkar, Kausik 2015 Hydrodynamic interactions between pairs of capsules and drops in a simple shear: Effects of viscosity ratio and heterogeneous collision. Phys. Rev. E 92 (6), 063029.

Sinha, Kushal & Graham, Michael D 2016 Shape-mediated margination and demargination in flowing multicomponent suspensions of deformable capsules. Soft Matter 12 (6), 1683–1700.

Smart, Jeffrey R & Leighton Jr, David T 1991 Measurement of the drift of a droplet due to the presence of a plane. Phys. Fluids A: Fluid Dyn. 3 (1), 21–28.

Sukumaran, Sreejith & Seifert, Udo 2001 Influence of shear flow on vesicles near a wall: a numerical study. Phys. Rev. E 64 (1), 011916.

Tan, Jifu, Thomas, Antony & Liu, Yaling 2012 Influence of red blood cells on nanoparticle targeted delivery in microcirculation. Soft Matter 8 (6), 1934–1946.

Tasciotti, Ennio, Liu, Xuewu, Bhavane, Rohan, Plant, Kevin, Leonard, Ashley D, Price, B Katherine, Cheng, Mark Ming-Cheng, Decuzzi, Paolo, Tour, James M, Robertson, Fredika & others 2008 Mesoporous silicon particles as a multistage delivery system for imaging and therapeutic applications. Nat. Nanotechnol. 3 (3), 151.

Vahidkhah, Koohyar & Bagchi, Prosenjit 2015 Microparticle shape effects on margination, near-wall dynamics and adhesion in a three-dimensional simulation of red blood cell suspension. Soft Matter 11 (11), 2097–2109.

Vlahovska, Petia M & Gracia, Ruben Serral 2007 Dynamics of a viscous vesicle in linear flows. Phys. Rev. E 75 (1), 016313.

Wootton, David M & Ku, David N 1999 Fluid mechanics of vascular systems, diseases, and thrombosis. Annu. Rev. Biomed. Eng. 1 (1), 299–329.

Ye, Huilin, Shen, Zhiqiang & Li, Ying 2018a Cell stiffness governs its adhesion dynamics on substrate under shear flow. IEEE Trans. Nanotechnol. 17 (3), 407–411.

Ye, Huilin, Shen, Zhiqiang & Li, Ying 2018b Computational modeling of magnetic particle margination within blood flow through lammps. Comput. Mech. 62 (3), 457–476.

Ye, Huilin, Shen, Zhiqiang, Yu, Le, Wei, Mei & Li, Ying 2017a Anomalous vascular dynamics of nanoworms within blood flow. ACS Biomater. Sci. Eng. 4 (1), 66–77.

Ye, Huilin, Shen, Zhiqiang, Yu, Le, Wei, Mei & Li, Ying 2018c Manipulating nanoparticle transport within blood flow through external forces: an exemplar of mechanics in nanomedicine. Proc. R. Soc. A 474 (2211), 20170845.

Ye, Huilin, Wei, Heng, Huang, Haibo & Lu, Xi-yun 2017b Two tandem flexible loops in a viscous flow. Phys. Fluids 29 (2), 021902.

Zhang, Junfeng, Johnson, Paul C & Popel, Aleksander S 2007 An immersed boundary lattice boltzmann approach to simulate deformable liquid capsules and its application to microscopic blood flows. Physical biology 4 (4), 285.

Zhang, Junfeng, Johnson, Paul C & Popel, Aleksander S 2008 Red blood cell aggregation and dissociation in shear flows simulated by lattice boltzmann method. J. Biomech. 41 (1), 47–55.

Zhao, Hong & Shaqfeh, Eric SG 2011 Shear-induced platelet margination in a microchannel. Phys. Rev. E 83 (6), 061924.

Zhao, Hong & Shaqfeh, Eric SG 2013 The dynamics of a non-dilute vesicle suspension in a simple shear flow. J. Fluid Mech. 725, 709–731.

Zhao, Hong, Shaqfeh, Eric SG & Narsimhan, Vivek 2012 Shear-induced particle migration and margination in a cellular suspension. Phys. Fluids 24 (1), 011902.

Zhao, Hong, Spann, Andrew P & Shaqfeh, Eric SG 2011 The dynamics of a vesicle in a wall-bound shear flow. Phys. Fluids 23 (12), 121901.